Development and Structure of Winter Monsoon Cloud Clusters on 10 December 1978[1]

DEAN D. CHURCHILL AND ROBERT A. HOUZE, JR.

Department of Atmospheric Sciences, University of Washington, Seattle, WA 98195

(Manuscript received 16 May 1983, in final form 19 December 1983)

ABSTRACT

Data from the Winter Monsoon Experiment (WMONEX) are used to study cloud clusters that occurred over the South China Sea on 10 December 1978. These clusters underwent life cycles in which they began as groups of intense convective cells and then developed into mesoscale systems consisting partly of convective cells and partly of stratiform precipitation. In the cellular regions of clusters, ice particle concentrations (at the 8 km, or −17°C, level) were found to be of the order of hundreds per liter, local convective updrafts of 4–17 m s^{-1} were observed, and the dominant ice-particle growth mechanism appeared to be riming. In the stratiform regions of clusters, the ice particles appeared to grow by vapor deposition and aggregation and weaker but more widespread mesoscale updraft motion was indicated at mid to upper levels by the observed ice-crystal structures, while unsaturated mesoscale downdraft motion was indicated at mid to lower levels by sounding data. The ice-particle concentrations at 8 km in stratiform regions were one to two orders of magnitude lower than in the convective regions; in areas of weaker stratiform precipitation the concentrations were 1–10 per liter, while in areas of stronger stratiform precipitation they were 20–70 per liter. Substructure within the stratiform regions was indicated by variations in observed ice-crystal habits over horizontal distances of 10–100 km.

The dominant cluster observed on this day was initiated when a group of convective cells formed just off the Borneo coast, apparently in response to land–breeze convergence. During the mature stage of this cluster, the stratiform rain area became nearly surrounded by a broken line of convective cells of various intensity. The greatest concentration of intense cores was maintained in a generally stationary region on the southeast side of the cluster where the land–breeze convergence was located, while convection on the northwest side of the cluster propagated out to sea. The stratiform precipitation area of this cluster appeared to be formed and maintained by a combination of three processes: dying convective cells being transformed into stratiform structures, hydrometeors being advected from the tops of active cells into the stratiform precipitation region and condensation in the mesoscale updraft contributing to the growth of hydrometeors falling as stratiform rain. About 46% of the total precipitation from this cluster fell as stratiform rain.

Other cloud clusters that occurred on this day generally formed around the periphery of the large land–breeze generated cluster and were of a smaller size. Convective downdraft outflows found in the regions between the old and new clusters may have been involved in triggering the new clusters.

1. Introduction

In previous studies based on data from the Global Atmospheric Research Program's Winter Monsoon Experiment (WMONEX), Houze *et al.* (1981b), Johnson and Priegnitz (1981) and Johnson (1982) have shown that winter monsoon clouds and precipitation over the "maritime continent" (i.e., Malaysia, Indonesia and surrounding seas) take place largely in mesoscale convective systems (or "cloud clusters") initiated by low-level convergence associated with local diurnal land–sea circulations. These cloud clusters exhibit a life cycle similar to those of mesoscale cloud systems found elsewhere in the tropics (Leary and Houze, 1979a; Houze and Betts, 1981; Houze, 1982). Houze and Hobbs (1982) further discussed the similarity of this life cycle to the life cycles of midlatitude convective complexes of the type described by Maddox (1980).

The typical cloud-cluster life cycle commences with the formation of a group of convective cells that evolves into a system composed of a combination of convective cells and mesoscale stratiform precipitation within the area covered by a mesoscale upper-level cloud shield observed by satellite. As the system ages, the precipitation becomes increasingly stratiform and less convective, then ceases. The upper-level cloud persists for several more hours, slowly thinning and finally dissipating.

Several aspects of this life cycle of a tropical cloud cluster need better understanding. In this paper we seek to confirm, refine and supplement the present view of the typical cloud cluster life cycle by an examination of a group of cloud clusters that occurred over the South China Sea during WMONEX on 10 December 1978. The dominant cluster on this day (referred to as cluster B) has been briefly described by Houze *et al.* (1981b) and Johnson and Priegnitz (1981) as an example of the type of mesoscale cloud system that forms diurnally off the coast of Borneo.[2] Warner

[1] Contribution No. 669, Department of Atmospheric Sciences, University of Washington.

[2] The island comprised of the Malaysian states Sarawak and Sabah, the four Indonesian Kalimantan provinces and Brunei is referred to in this paper by the geographical name Borneo.

(1982) has also described this cluster. Three clusters (including B) were penetrated by a research aircraft equipped with quantitative radar, cloud microphysical instrumentation and dropwindsondes. These airborne observations document for the first time the microphysical structure of tropical cloud clusters above the 0°C level. Together with measurements obtained with a quantitative radar on the coast of Borneo, surface and upper air data from ships and geosynchronous satellite imagery, these data form a comprehensive set documenting the structure and development of winter monsoon cloud clusters.

2. Observational network and description of the data

Figure 1 shows the WMONEX data collection network on 10 December 1978. Three Soviet research ships in the South China Sea formed a triangle north of Borneo. A weather radar from the Massachusetts Institute of Technology (MIT) was located at Bintulu on the north coast of Borneo. The effective area of coverage of the radar is indicated by the partial circle surrounding Bintulu in Fig. 1. The WP-3D aircraft from the National Oceanic and Atmospheric Administration (NOAA), hereafter referred to as the "P3", and the Electra research aircraft from the National Center for Atmospheric Research (NCAR) flew missions over the South China Sea at altitudes of 7.8 and 6.3 km respectively. Their flight tracks are indicated in Fig. 1.

The Japanese geosynchronous satellite GMS-1 obtained infrared and visible imagery during WMONEX, and digitized visible and infrared brightness imagery of the research area on 9 and 10 December 1978 were used in this study. (Data provided by the Space Sciences and Engineering Center (SSEC), University of Wisconsin, Madison, WI 53706.) The horizontal resolution was 2.5 km for the digitized visible imagery and 5.0 km for the infrared.

Surface and upper air charts for 0000 and 1200 GMT were obtained from the WMONEX Quick-look Data Set (available through the FGGE Data Catalogue, World Data Center-A, Federal Building, Asheville, NC 28801) and from Chang *et al.* (1981). Digital records of surface and rawinsonde observations at the Soviet research ships were also obtained from Asheville.

The MIT radar system, used previously on board the R.V. *Gilliss* during GATE (Arkell and Hudlow, 1977; Hudlow *et al.*, 1979), is controlled by a computer which directs the antenna, digitizes the returned signals and records the data on magnetic tape. In WMONEX the antenna ran through a prescribed sequence of conical scans that was repeated every 10 min. Magnetic tapes, containing calibrated integral values of radar reflectivity in units of dBZ (dBZ = 10 log$Z$, where Z is the equivalent radar reflectivity factor) mapped into Cartesian coordinates, were generated at MIT after the experiment. These maps, which have 4 km horizontal resolution and 2 km vertical resolution, were used to study the development of precipitation associated with cloud cluster B. Reflectivity data from the MIT radar were converted to rainfall rate using the relationship $Z = 230R^{1.25}$, where Z is the equivalent radar reflectivity factor in mm^6 m^{-3} and R is the rainfall rate in mm h^{-1}. This relationship was developed for GATE by Hudlow *et al.* (1979) and, for our purpose, is not significantly different from the refined GATE Z–R relationship determined by Austin and Geotis (1979).

The P3 aircraft was also equipped with a C-band weather radar, mounted beneath the fuselage, which provided reflectivity data throughout the mission on 10 December 1978. (Nose and tail radars are also located on the P3 but were not used in this study.) The lower fuselage radar scanned 360 deg horizontally every 15 s and every other scan was digitally recorded. (These data tapes are stored in the Department of Atmospheric Sciences, University of Washington, Seattle, WA 98195.) Houze *et al.* (1981a) tested the accuracy of the lower fuselage radar by comparing its images with those of the MIT radar and found that the data from the two radars agreed to within 2 dBZ.

Digitized ice particle images were obtained on board the P3 with Particle Measurement System (PMS) probes (Knollenberg, 1970). The "cloud probe" detected shadowgrams of particles up to 1.6 mm in diameter, while the "precipitation probe" detected sizes up to 5 mm. The precipitation probe data were not used in this paper. For details on the operation, characteristics and use of these types of probes, see Cannon (1976), Heymsfield (1976) and Houze *et al.* (1981a). The habits and size spectra of particles provided by these data reveal particle nucleating temperatures and growth mechanisms. The particle image data and methods used to analyze them are discussed in the Appendix.

Both the NCAR Electra and the P3 were equipped with dropwindsondes (Julian, 1982) which provided soundings of temperature, humidity and wind. (Data supplied by the former MONEX Project Office, National Center for Atmospheric Research, and the FGGE Data Catalogue.) Winds were determined by tracking the falling instrument package using standard Omega navigational signals. The aircraft flight-level parameters used in this study were 1 s averages of time, latitude, longitude, radar altitude, temperature, dew point, vertical wind speed and cloud liquid water content. On the P3, cloud liquid water content was measured with a Johnson-Williams hot wire device (Ruskin, 1976).

3. Synoptic conditions and overview cloud cluster evolution

The 10th of December was characterized by the onset of a "cold surge" over the South China Sea. During a cold surge, northeasterly monsoon surface winds over the South China Sea increase in speed in conjunction with the passage of an upper-level trough in central China, and cloudiness and precipitation are enhanced along the north coast of Borneo (Ramage, 1971; Chang *et al.*, 1979; Chang and Lau, 1980; Houze

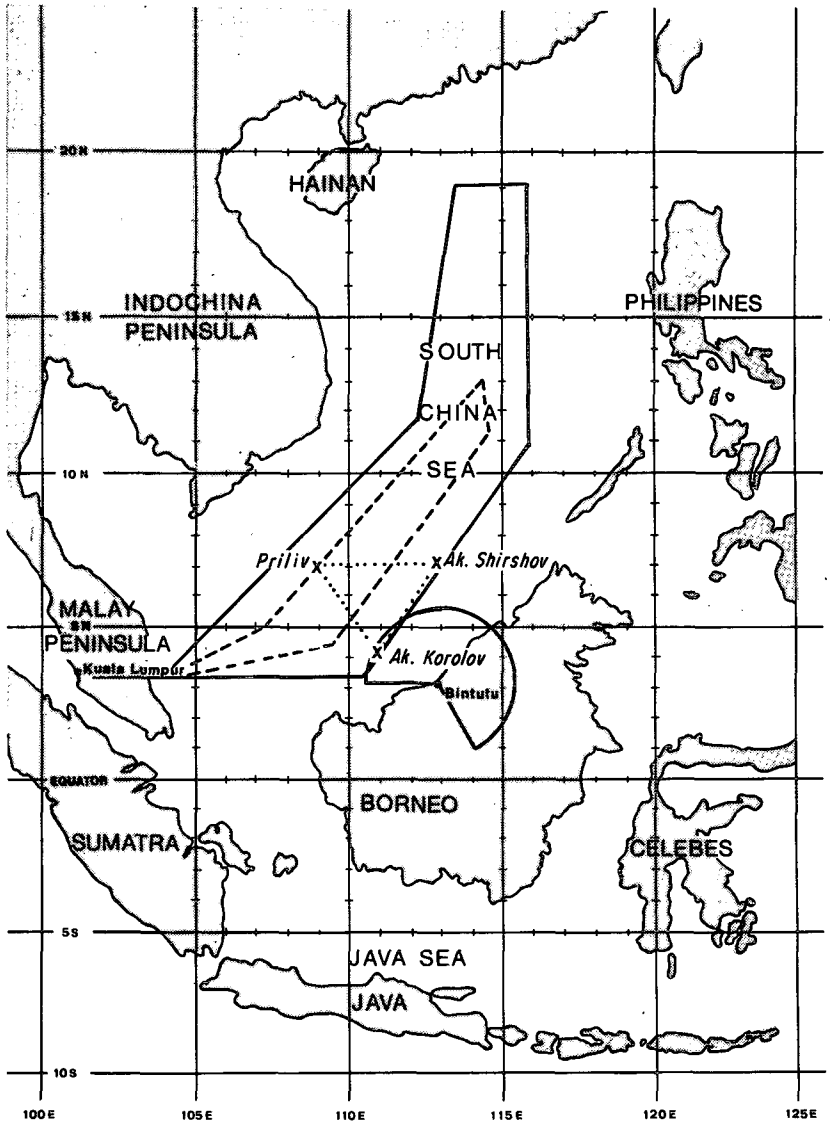

FIG. 1. WMONEX data network on 10 December 1978. The flight tracks of the P3 (heavy solid line) and the Electra (dashed line) are shown. The Soviet ship positions are indicated by crosses with the ship names beside them. The region of land-based radar coverage around Bintulu, about 3.2°N, 113.1°E, on the northern coast of Borneo is indicated by a solid line surrounding Bintulu. The southwestern sector of the radar coverage was obstructed.

et al., 1981b; Johnson and Priegnitz, 1981). At 0000 GMT 10 December 1978, 15 m s^{-1} northeasterly surface winds over the South China Sea extended southward to 6°N (Fig. 2a). By 1200 GMT they reached 1°N (Fig. 2b), indicating the intensifying cold surge. At middle and upper levels the flow was easterly over the north coast of Borneo, in a pattern typical of the winter monsoon (Figs. 3 and 4).

Satellite imagery of the upper-level cloudiness in the vicinity of Borneo from 1733 GMT[3] 9 December to 1530 GMT 10 December is shown in Fig. 5. The corresponding schematics in Fig. 6 show the evolution of the family of cloud clusters (labeled A–J) that developed along the north coast of Borneo and over the South China Sea.

Clusters A, B and C were penetrated by the P3 aircraft between 0900 and 1100 GMT (the progression of the flight track is indicated in Figs. 6i–k). Low-level convergence centered near 3.5°N, 114°E (Fig. 2a) and an apparent increase in upper-level difluence over the north coast of Borneo between 0000 and 1200 GMT (Fig. 4) were consistent with the development of this group of cloud clusters.

[3] On Borneo, Greenwich Mean Time equals Local Standard Time plus 8 h: GMT = LST (at 112.5°E) + 7.5 h.

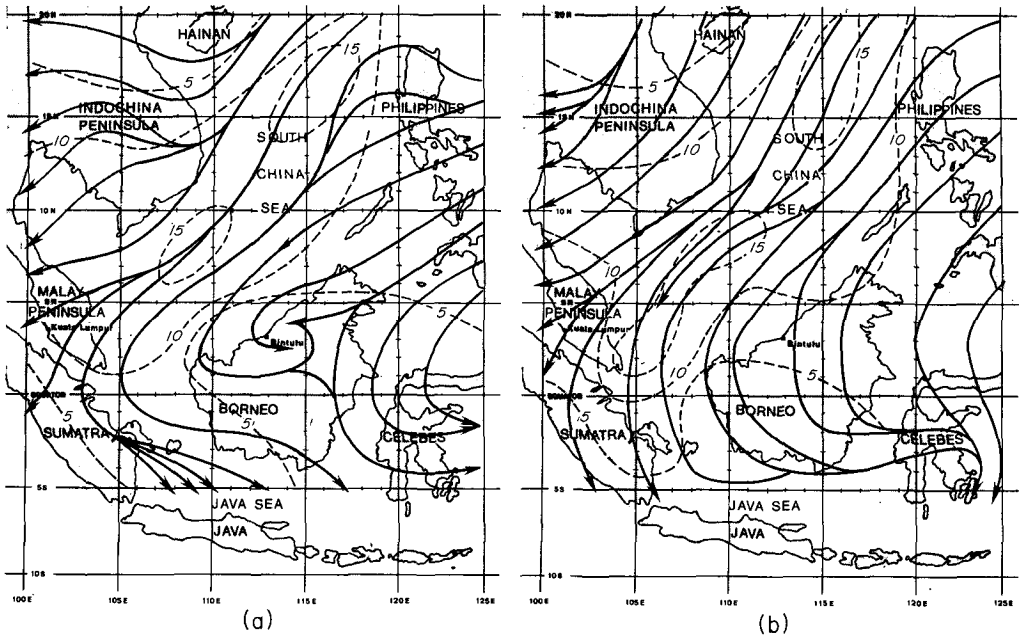

FIG. 2. Surface streamlines and isotachs (m s^{-1}) for (a) 0000 and (b) 1200 GMT 10 December 1978. Adapted from Chang *et al.* (1981).

Cluster B dominated the family of clusters depicted in Fig. 6. It was apparently triggered by the low-level convergence of the diurnal land breeze with the northeasterly monsoonal surface flow just off the north coast of Borneo. After 1730 GMT, cluster B grew until the area covered by its cirrus shield reached a maximum at about 0530 GMT (Figs. 6a–h). During this period of growth, the southeastern boundary of the cirrus shield was stationary along the coast of Borneo while the western and northern boundaries expanded outward. Cluster I, also seen developing at 1733 GMT (Fig. 6a), never attained as great an areal extent as B. By about 2300 GMT, while cluster B was still actively expanding, cluster I was decreasing in size.

Extensive changes occurred in the cloud patterns between 0233 and 0833 GMT (Figs. 6g–i). Cluster B developed a northern arm connecting with the remains of cluster I, while separate new clusters, A, C and J, formed. During the next three hours (Figs. 6i–k), clusters A, B and C were penetrated by the P3. Active growth continued to occur on the western, northern and northeastern borders of B during this time. However, at about the time the typical diurnal low-level flow reversed from offshore to onshore (Fig. 8 of Houze *et al.*, 1981b), the southeastern border of B disintegrated, while new clusters D, E, F, G and H appeared just inland from the coastline. (Note a similar behavior over the Makassar Strait along the east coast of Borneo, where new clusters also formed in a line just inland from the edge of a weakening cluster (Figs. 5g–i).)

Subsequent sections of this paper describe the aircraft penetrations of clusters A–C, supported by the land-based radar observations of B and satellite and ship data. These descriptions elucidate the internal structure of these clusters at various stages of development, while observations obtained in the regions between A, B and C help reveal the nature of the influence of B on the subsequent development of clusters A and C.

4. Cloud cluster A

a. Satellite and radar data

The area covered by the cirrus shield[4] and the minimum cloud top temperature of cluster A were determined as functions of time from the digitized satellite infrared data (Fig. 7). These data might indicate that the cluster was penetrated during an expanding stage of development, since its areal growth rate was maximum. However, its deepest convection, indicated by a minimum cloud top temperature of −75°C, had occurred 1–2 h before the P3 penetration and a mesoscale rain area, indicated by a radar echo 3.26×10^3 km^2 in area (point × in Fig. 7), had already developed. The echo, shown in Fig. 8 inside the boundary of the satellite-detected cirrus shield, consisted of a region of convective echo cells, two of which had peak reflectivity factors over 40 dBZ, and a relatively uniform area

[4] A cloud top threshold temperature of −26°C (247 K) was applied to the infrared data to determine cloud area. This limit yielded areas that agreed well with visual estimates, using infrared images, of the areal extent of cluster A's cirrus shield.

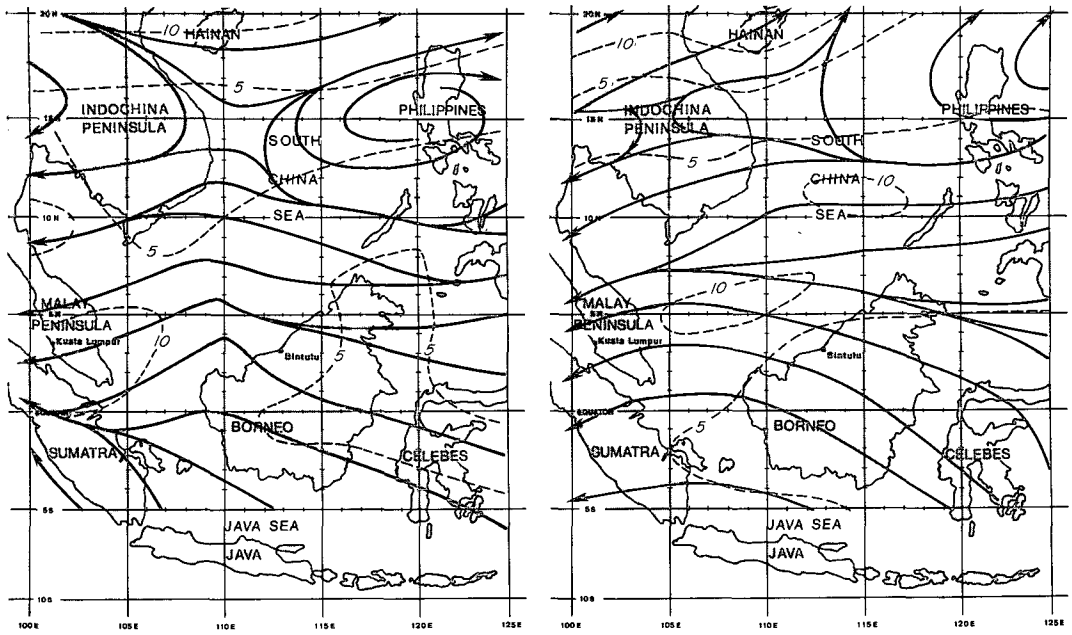

FIG. 3. Streamlines and isotachs (m s^{-1}) at 500 mb for (a) 0000 and (b) 1200 GMT 10 December 1978. Adapted from Chang *et al.* (1981).

(approximately 2×10^3 km^2) of stratiform precipitation, with reflectivity values of 20–23 dBZ. It appears from Figs. 7 and 8 that this cloud cluster was characterized by the typical life cycle discussed in the Introduction, and that, by the time of the P3 penetration, the mesoscale rain area had reached the mature stage in which convective and stratiform precipitation coexisted.

Cloud and weather observations reported from *Ak. Shirshov,* located beneath cluster A (see ship position

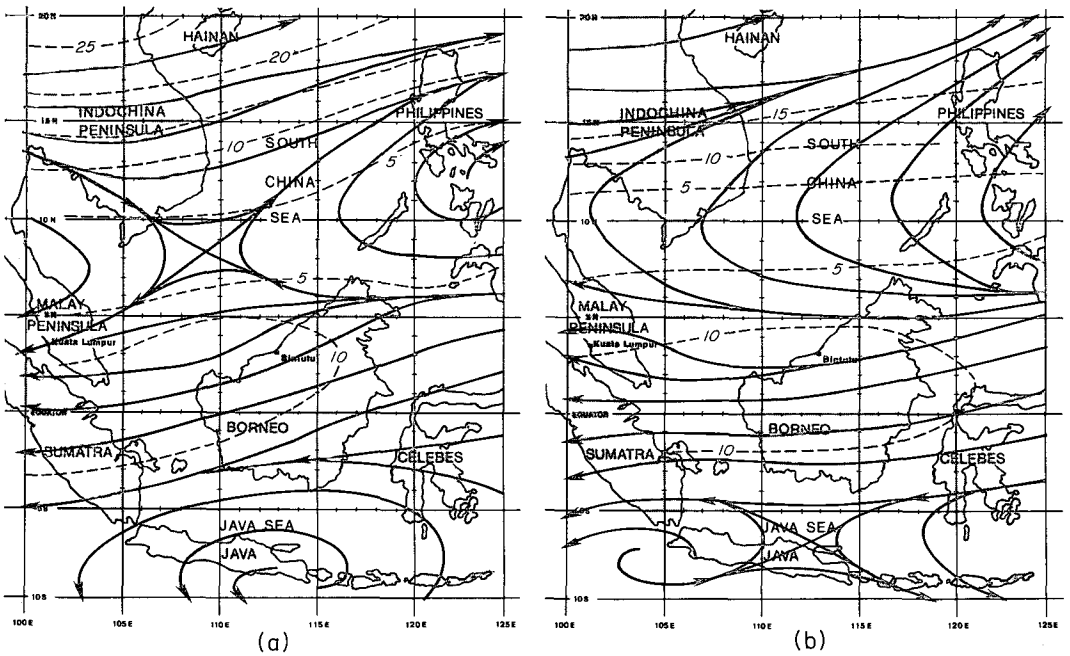

FIG. 4. Streamlines and isotachs (m s^{-1}) at 200 mb for (a) 0000 and (b) 1200 GMT 10 December 1978. Adapted from the Winter MONEX Quick-Look Data Set.

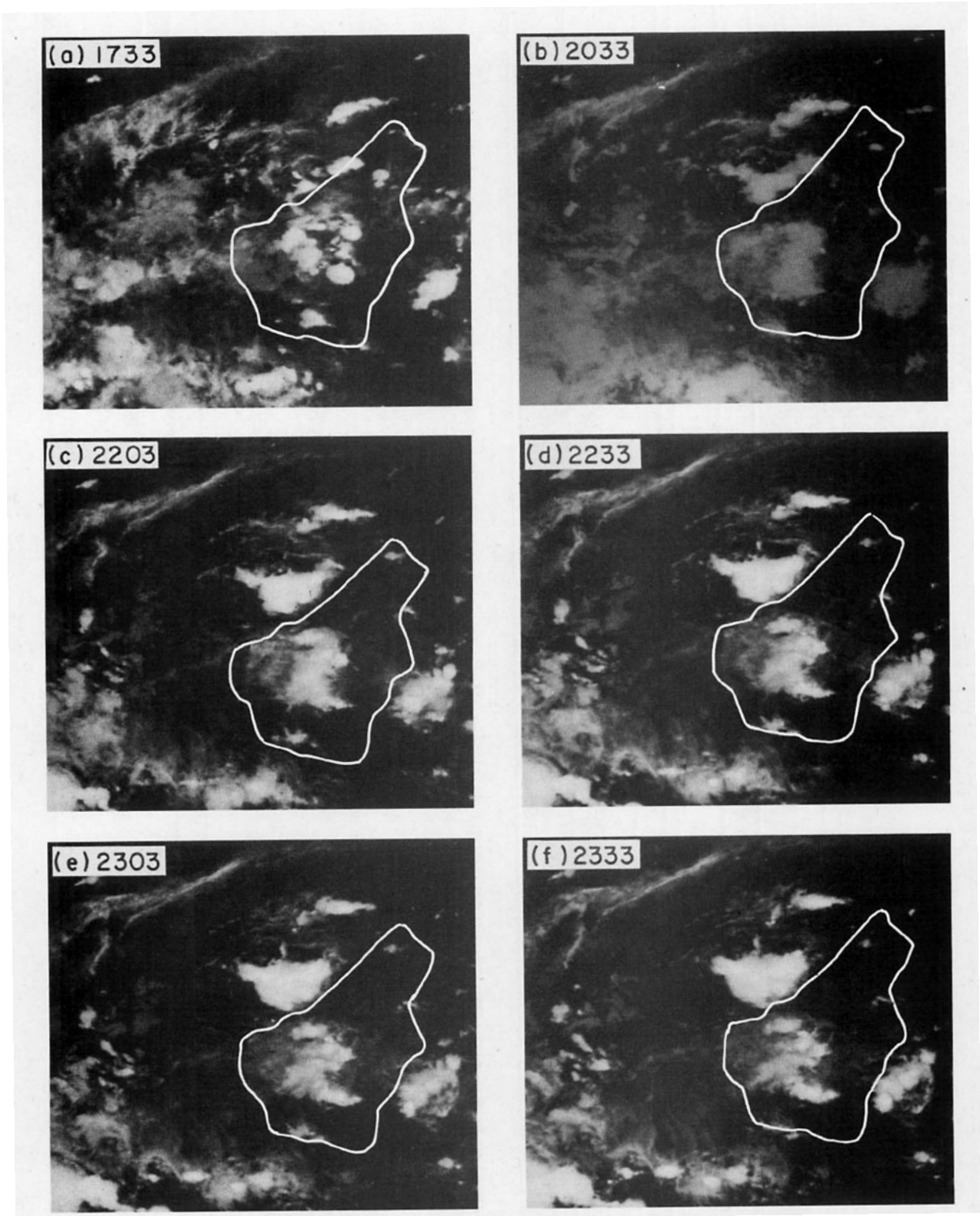

FIG. 5. Infrared satellite images, showing cloud clusters over the South China Sea and Borneo. Part (a) is for 1733 GMT 9 December 1978. The sequence proceeds through part (n) at 1533 GMT 10 December 1978.

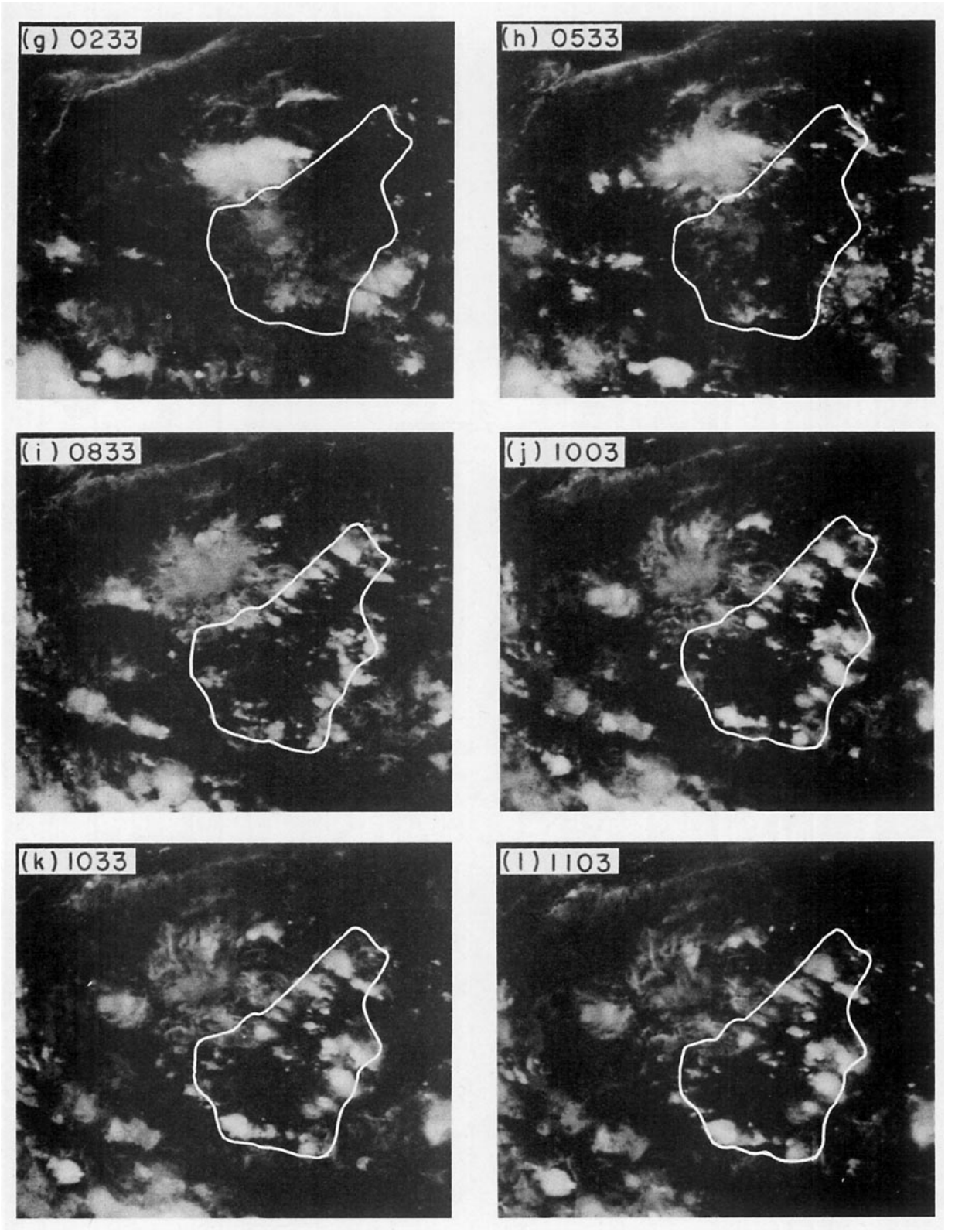

FIG 5. (*Continued*)

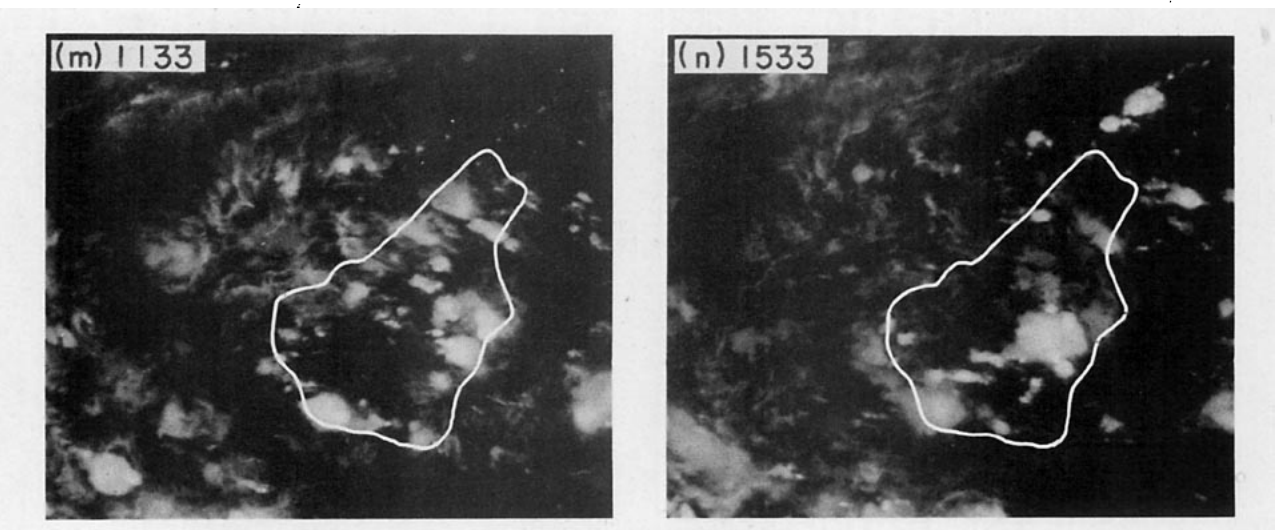

FIG. 5. (*Continued*)

in Fig. 8), were consistent with such a life cycle (Fig. 9). From 0500 to 0700 GMT *Ak. Shirshov* reported building cumulus evolving into cumulonimbus with cirriform tops. A moderate rainshower had begun by 0700 GMT and 0.9 of the sky was covered by low- and middle-level cloud. At 0800 GMT heavy thunderstorm activity was reported (the same time as the lowest minimum cloud top temperature in Fig. 7). By 0900 GMT, the thunderstorm had ended, though some rain fell at the ship during the next hour. From 0900 to 1100 GMT, the ship reported middle cloud and cirrus, presumably the cloud deck of A, combined with cumulonimbus covering 0.9 of the sky. Throughout the period of 1100–1200 GMT rain was seen reaching the sea in the distance, but not at the ship. At 1200 GMT *Ak. Shirshov* recorded a 6 h precipitation total of 11 mm. Then, a clearing trend brought fair weather for the next few hours.

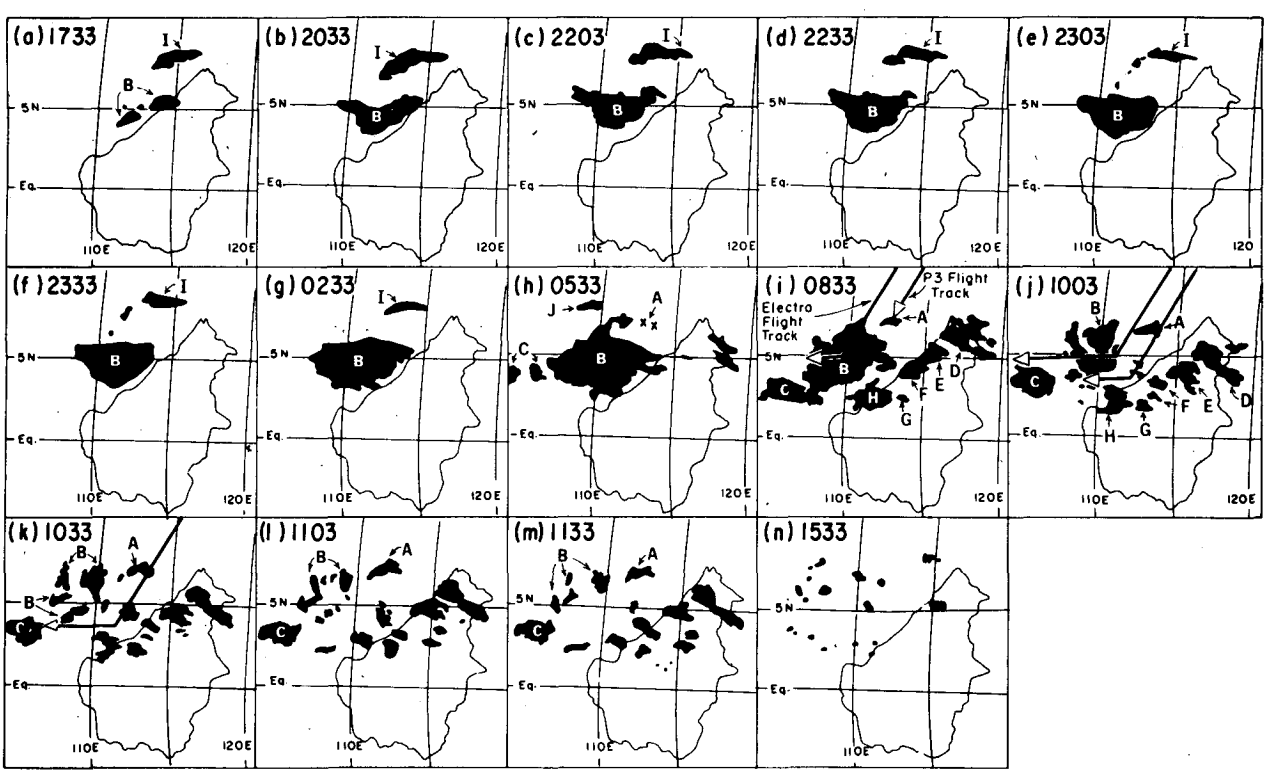

FIG. 6. Schematics of infrared satellite imagery. The cloud clusters seen in boundaries were determined by the 247 K threshold.

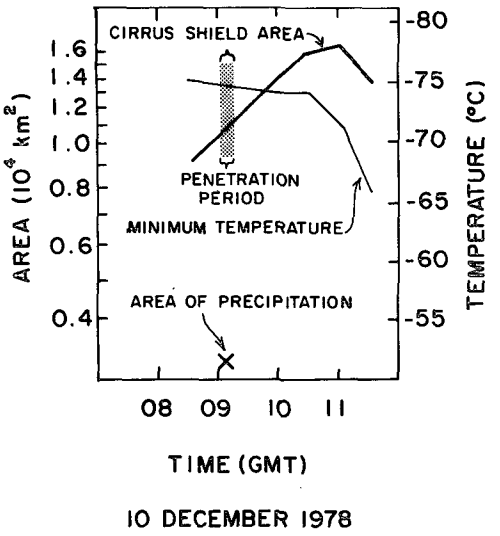

FIG. 7. Cirrus shield area, precipitation area and minimum cloud top temperature for cluster A. The area covered by the cirrus shield (thick curve), and the minimum cloud top temperature (thin curve) were determined from infrared satellite imagery. The area covered by precipitation (at 0902 GMT, indicated by the cross) was determined from the P3's lower fuselage radar using a 1 dBZ threshold. The shaded column indicates the period during which the P3 was in the cluster.

b. Cloud patterns around the cluster

The overlaid patterns of satellite and radar data of Fig. 8 are shown in Fig. 10 on a larger scale map, which also shows schematically cloud patterns determined by photographs taken aboard the aircraft and by high resolution satellite imagery. Also shown in Fig. 10 are surface observations, the position of *Ak. Shirshov,* the flight track, dropwindsonde locations and the vantage points and viewing angles of the photographs taken from the aircraft.

The aircraft photographs on which the cloud patterns in Fig. 10 are based are shown in Figs. 11–13. Fig. 11a is a view from 250 km northeast of cluster A. The schematic in Fig. 11b indicates the observed cloud types. In the background, the cumulonimbus (Cb) comprising cluster A filled most of the horizon and extended from below to above flight level. Thin cirrus (Ci) and cirrostratus (Cs) covered the whole sky with heights ranging from 11 to 15 km. In the foreground, below flight level, streets of small cumulus occurred in the boundary layer far from the cluster, while mediocris and congestus penetrated into the middle troposphere nearer the cluster (Warner, 1982).

In contrast to this pattern of clouds, a mosaic (Fig. 12) of the low-level cloudiness southwest of cluster A,

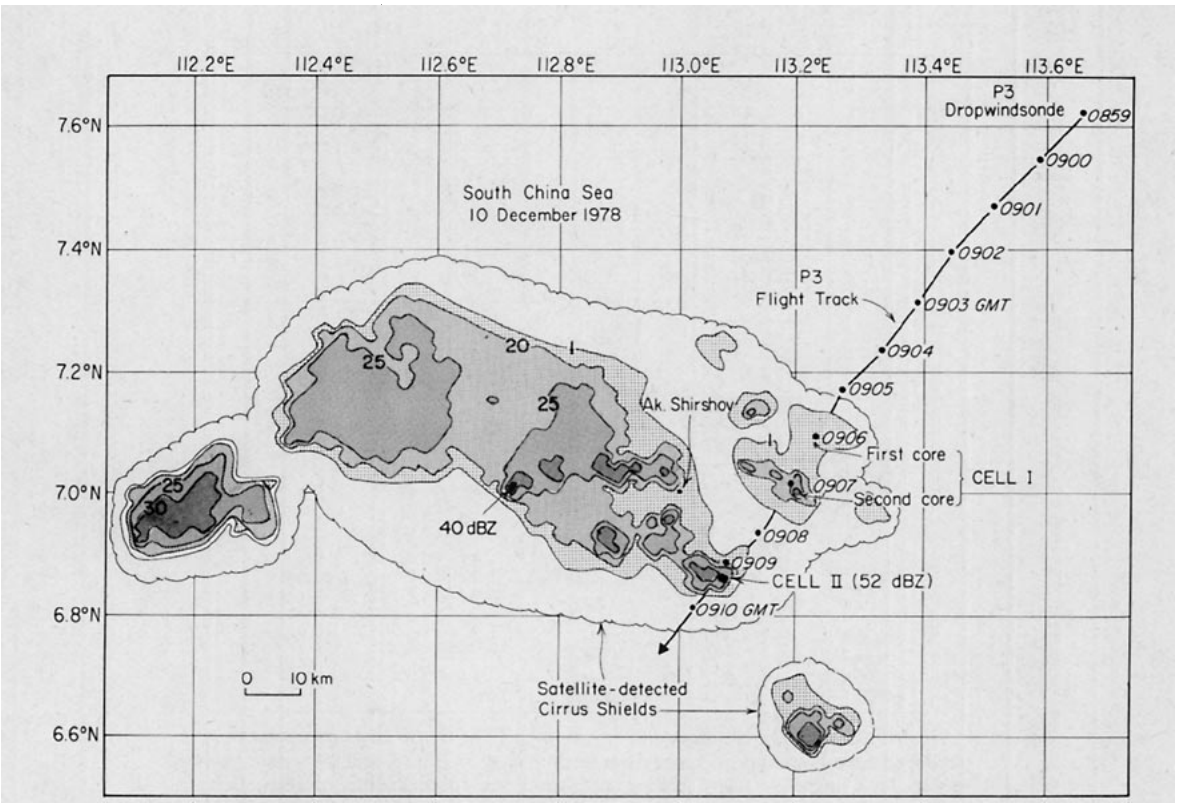

FIG. 8. Radar and satellite depiction of cluster A. The scalloped outline indicates the approximate boundary of the cloud shield seen in the satellite imagery (Figs. 5i and j). The contours indicate precipitation at 1, 20, 25, 30 and 40 dBZ detected by the P3's lower fuselage radar at 0908 GMT. The flight track of the P3 is annotated with time (GMT) to indicate the aircraft position. The two convective cells penetrated by the P3 are labeled I and II. The flight level was 7.8 km.

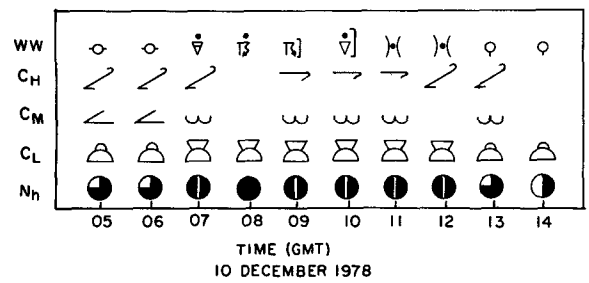

FIG. 9. Clouds and weather beneath cluster A, reported by the ship *Ak. Shirshov*. The top row shows the current weather (WW), the second shows the high clouds (C_H), the third shows the middle clouds (C_M), the fourth shows the low clouds (C_L) and the bottom row shows the fraction of the sky covered by low- and middle-level clouds (N_h).

photographed after the P3 completed its penetration, shows four distinct suppressed regions; the cloud lines between them appear similar to the areas described by Warner *et al.* (1979). On the left (west), cloud streets, not unlike those observed the same day in higher latitudes of the South China Sea (Warner, 1982), indicated a region of undisturbed air. The suppressed areas, which had patches of stratus of little vertical extent and laminar appearance, were probably associated with pools of low wet-bulb potential temperature (θ_w) air which originated as convective downdraft outflow from clusters A and B. At the boundaries of these outflows, arc lines of low-level cumulus formed. Fig. 13 looking east-northeast at 0920 GMT, shows another suppressed region south of cluster A, with arc lines and towering cumulus in the distance. Enhanced visible satellite imagery (Fig. 14) shows arc lines along the southern edge of cluster A at 0833 GMT similar to the pattern of arc lines seen from the aircraft (Figs. 12 and 13). Despite the 45 min difference between the times of Figs. 12–13 and 14, there is good agreement between the aircraft photos and the satellite imagery.

c. *Formation of the cluster*

In Fig. 6h, it is noted that cluster A was forming between cluster B and the remnants of cluster I at 0533 GMT. Surface and sounding data taken at *Ak. Shirshov* suggest that convective downdraft outflows similar to those that appeared to produce the cloud arc lines described in Section 4b may have been involved in triggering cluster A. The hourly surface data at the ship showed a drop in wet-bulb potential temperature from 298.5 to 296.5 K between 0600 and 0700 GMT. The ship sounding reported for 0600 GMT (Fig. 15a)

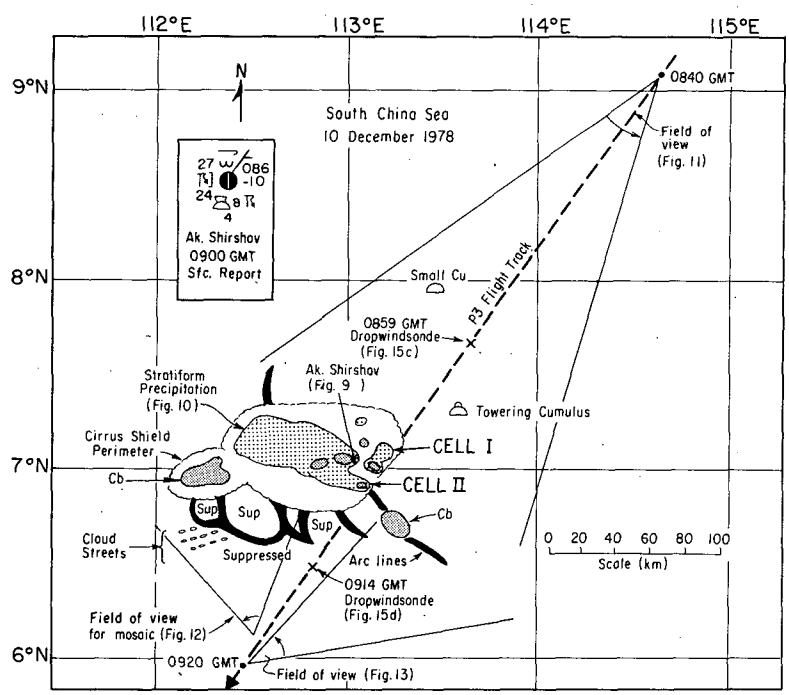

FIG. 10. Summary of cluster A and environment. The cirrus shield perimeter of A (scalloped curve) was approximated from satellite imagery (Fig. 6) and the photograph in Fig. 11. Convective (light shading) and stratiform (dark shading) precipitation, determined from airborne radar measurements, are bounded by a 1 dBZ contour. Small and towering cumulus are indicated northeast of A while positions of cloud streets, arc lines and suppressed areas are shown southwest of A. The inset shows the *Ak. Shirshov* 0900 GMT surface report. Dropwindsonde locations along the flight track are labeled with crosses. The two convective cells penetrated by the P3 are labeled I and II. Figure numbers refer to further descriptions of data in Section 4.

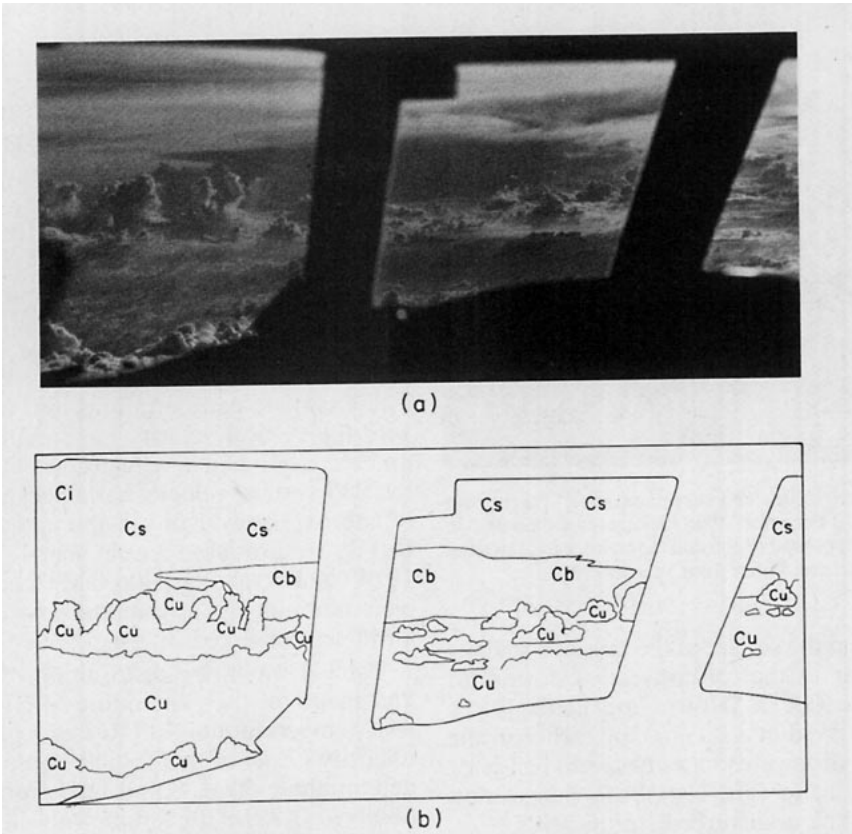

FIG. 11. (a) Clouds of cluster A. This photograph, taken from the cockpit of the P3 looking toward 213 deg at 0840 GMT 10 December 1978 shows the clouds associated with cluster A shortly before the P3 penetrated the cluster. Photo by R. A. Houze, Jr. (b) Nephanalysis, illustrating the clouds in (a). Conventional abbreviations identify the cloud formations.

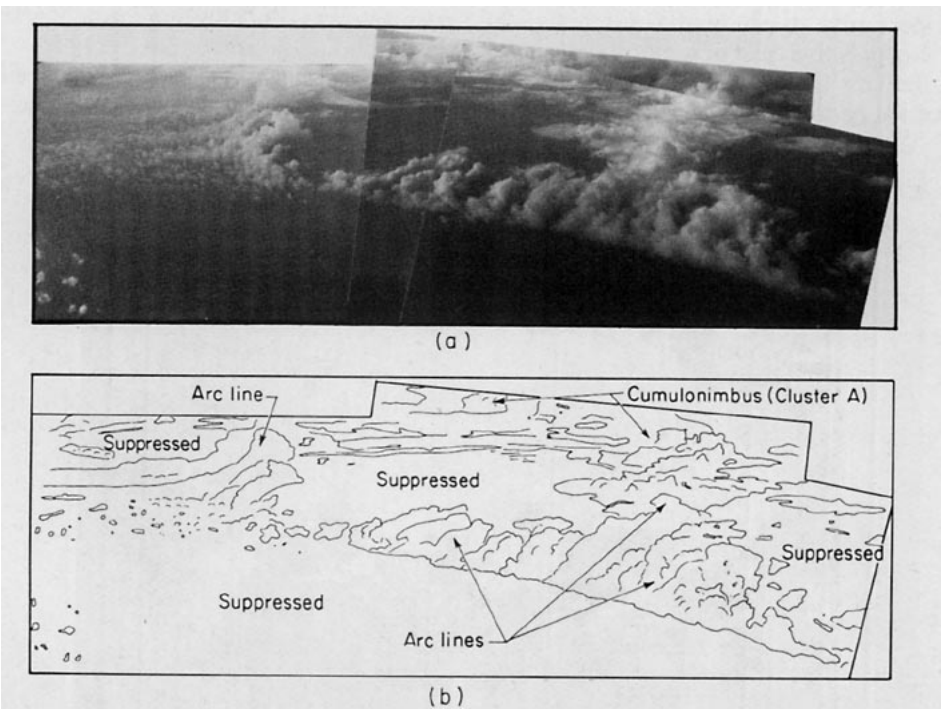

FIG. 12. (a) Mosaic of photos taken from the P3 looking toward 310 deg at 0917 GMT. These photos show arc lines and suppressed, nearly cloud-free areas west of cluster A. See Fig. 10 for the position of the aircraft at this time. Photo by R. A. Houze, Jr. (b) Nephanalysis of the clouds in (a). Suppressed areas and arc lines are identified. At the top of the figure, the bases of the cumulus congestus associated with cluster A are evident. See Fig. 10 for a planar view of this.

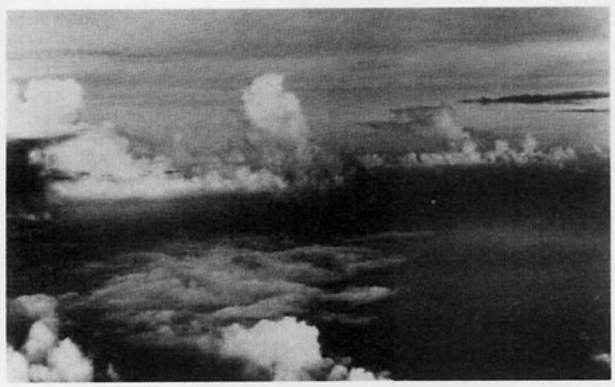

FIG. 13. Photo of arc clouds and suppressed area. Taken from the P3 at 0920 GMT 10 December 1978 looking toward 60 deg. In the foreground is the suppressed region and the arclines and towering cumulus are in the distance. Photo from Warner (1982).

showed the low θ_w at the surface at the base of a shallow stable layer similar to that of convective downdraft outflow air seen in GATE (Houze and Betts, 1981). The sounding observed at *Ak. Shirshov* earlier in the day (Fig. 15b) and dropwindsondes obtained just prior to (Fig. 15c) and just after (Fig. 15d) the P3 penetration of cluster A show the undisturbed stratification.

d. Microphysical structure and vertical motions

From Figs. 8 and 10, it is evident that the P3 flew through the convective region of cluster A. This afforded the opportunity to study the microphysical structure of the convective cells of a mature cluster at 8 km altitude. Between 0905 and 0910 GMT, the PMS probes detected ice particles as the P3 penetrated two convective cells over a distance of 50 km (the aircraft's speed was $\sim$10 km min^{-1}). Fig. 16 summarizes the ice-particle concentrations from the cloud probe and vertical velocities observed by the P3. The particle concentrations correlated well with the radar observations shown in Fig. 8. The maxima in Fig. 16 at 0906 and 0907 GMT occurred within cell I of Fig. 8, while the maxima just after 0909 GMT corresponded to cell II. The maximum concentration in cell I was 548 per liter, while cell II had a peak of 379 per liter. These particle concentrations also corresponded well with the vertical velocity measurements, with strong updrafts tending to have high concentrations. Although the P3's vertical velocity has a background noise level of approximately 1 m s^{-1}, the updrafts in cells I and II (Fig. 16) produced a clear signal. Peak velocities at 10, 40 and 50 s after 0906 GMT occurred during the penetration of cell I, while the peak at 20 s after 0909 GMT was observed in cell II.

Table 1 shows the distribution of particles by size and shape for the penetration of cluster A at a flight level temperature of -17°C (see Appendix). The vast majority (96%) of the particles were small and of indeterminable shape. Some nearly round particles were observed (1.8% of the sample) as well as a few medium and large indeterminable particles (2.2%). Since the on-board cloud physicist saw soft hail hitting the windshield of the aircraft in cell II, where the radar reflectivity reached 52 dBZ (Fig. 8), and given the strong updrafts (17 m s^{-1}), we believe that the nearly round particles were probably a mixture of graupel and small hail. It should be noted that the 17 m s^{-1} vertical wind speed is questionable in its accuracy since such large values are rare over tropical oceans (LeMone and Zip-

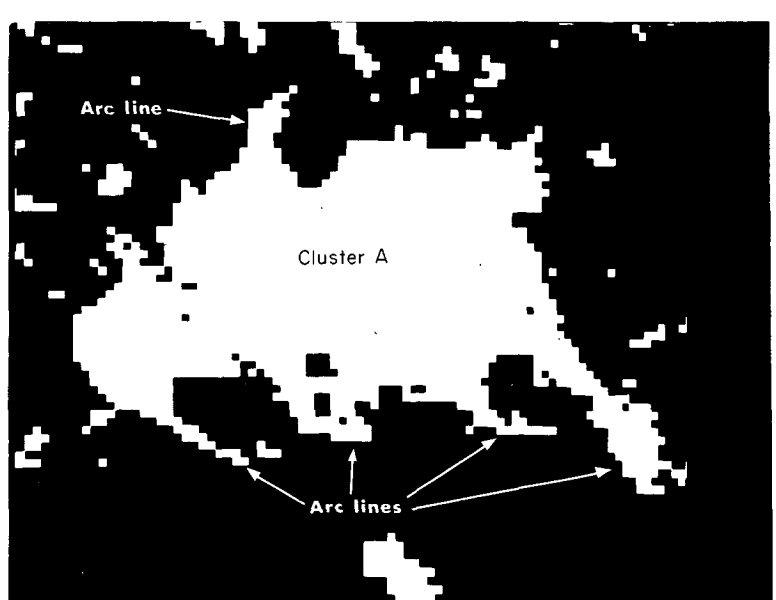

FIG. 14. Enhanced visible-light image of cluster A, 0833 GMT 10 December 1978. Arc lines are evident along the southern and northern edges of the cluster.

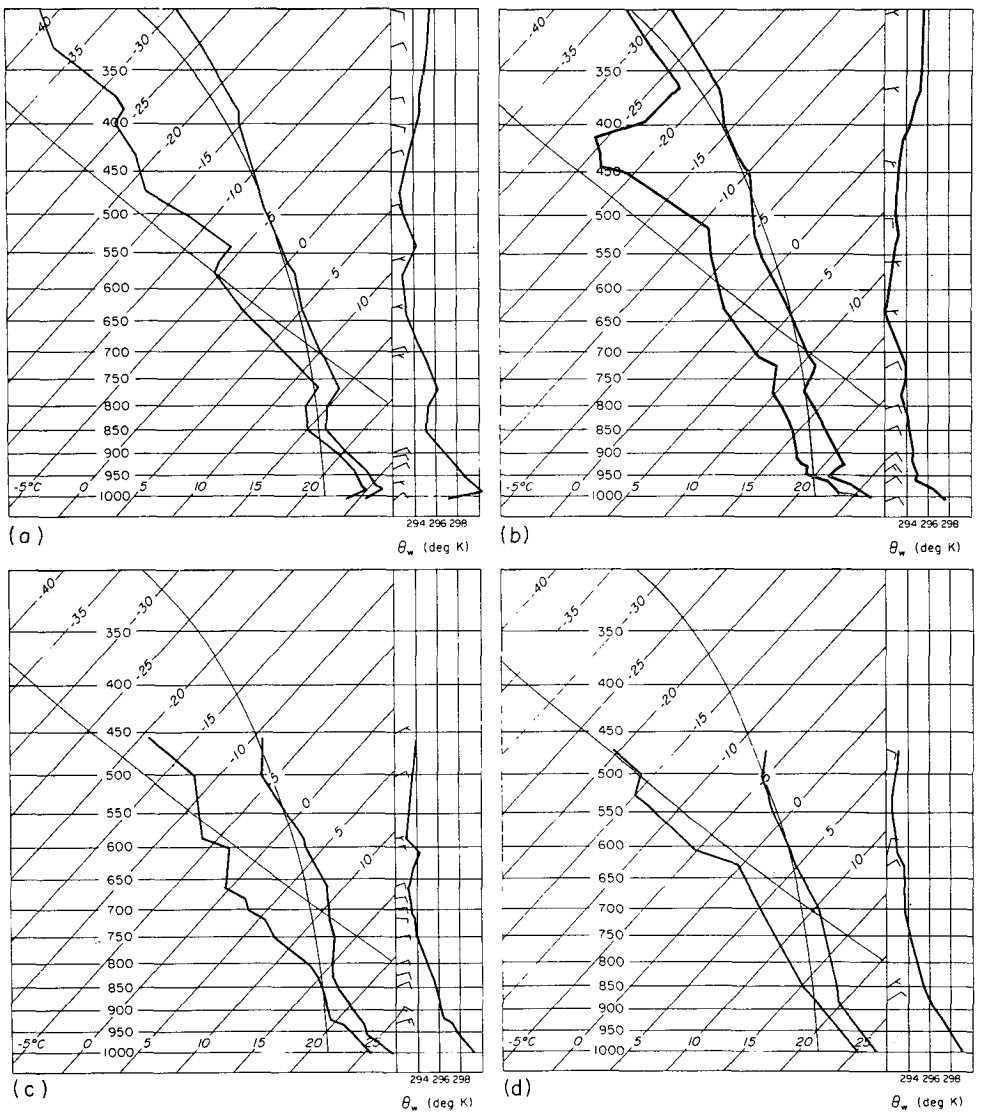

FIG. 15. Environmental and mean soundings for cluster A: (a) *Ak. Shirshov* sounding for 0600 GMT 10 December 1978; (b) *Ak. Shirshov* 0000 GMT; (c) P3 dropwindsonde at 0859 GMT, released at 7.62°N, 113.59°E; and (d) P3 dropwindsonde, 0914 GMT, released at 6.41°N, 112.78°E. Solid curves show temperature, dew point and wet bulb equivalent potential temperature (θ_w). Barbs show wind speed (one full barb 5 m s^{-1}) and direction.

ser, 1980; Zipser and LeMone, 1980). Qualitatively, however, this value is consistent with all of the other observations in indicating very strong convection.

The complete absence of vapor-grown habits (columns and branched crystals) in the cells implies that riming was the dominant particle growth mechanism. The indeterminable particles of all sizes were probably rimed particls. Heavily rimed particles are characteristic of convective cells and are consistent with the presence of strong updrafts (see Section 3a of Matejka *et al.*, 1980, for a discussion of dynamical inference from microphysical data).

During the penetration of the cells in cluster A, the peak 1 s average liquid water contents were 0.2 g m^{-3} and were found in peak updrafts. These rather low liquid water contents suggest that riming occurred below flight level and that convective updrafts lifted the particles to flight level.

5. Cloud cluster B

a. Overall cloud and precipitation coverage

The area covered by the cirrus shield and radar echo and the minimum cloud top temperature of cluster B are shown in Fig. 17 as functions of time, beginning at about 1730 GMT, just after B had formed. The deepest convection, as indicated by the minimum cloud top temperature, occurred at 2000 GMT, during the

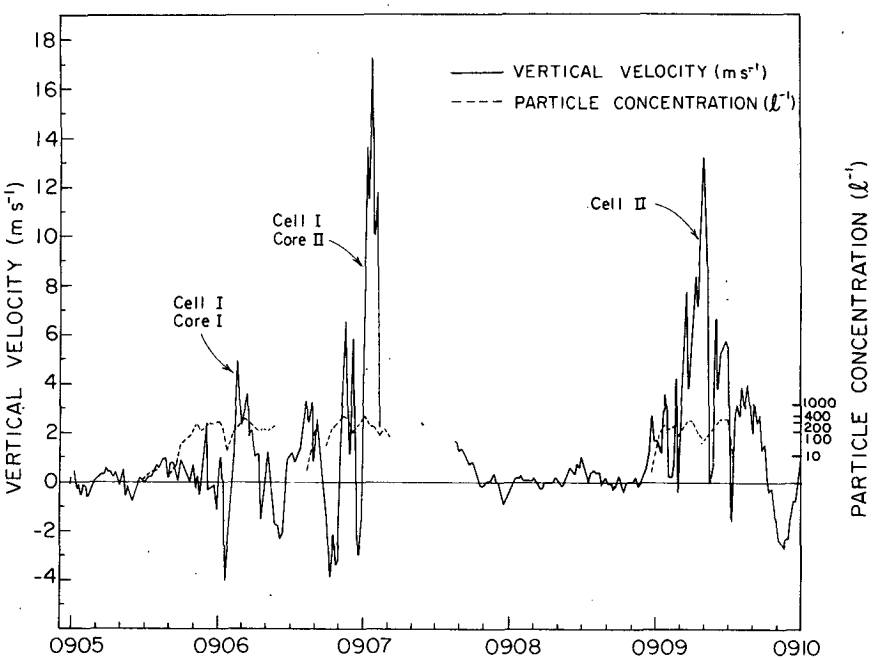

FIG. 16. Vertical velocity (solid line, m s^{-1}) and logarithm of cloud-ice particle concentration per liter in cluster A. The vertical velocities are 1 s averages determined by the P3's inertial navigation system. The particle concentrations are 2 s (0.3 km) averages determined from the Knollenberg cloud probe. Gaps in the particle concentration indicate zero ice particles. The gap in the vertical velocity trace was due to a data loss.

formative stage of development. The early to middle stages of this cluster were documented by the land-based radar at Bintulu and during its later stages it was penetrated by the P3 aircraft. The following subsections describe the detailed data obtained.

b. *Identification of internal structural features in radar echo patterns*

To examine the evolution of the internal structure of the cloud clusters, we have subdivided the precipitation area seen on radar into convective and stratiform regions. Fig. 18 shows a sequence of six maps depicting the echo patterns at 3 km altitude obtained by the Bintulu radar at 2 h intervals. Stratiform precipitation is indicated by light shading, while convective rain is indicated by dark shading. Within the convective areas, symbols locate convective cores and indicate their dBZ values, with dots representing values of 1–20 dBZ, plus signs representing 21–30 dBZ, squares 31–40 dBZ and triangles 41 dBZ or above. The method for identifying convective echo cores and partitioning the reflectivity field into convective and stratiform components is similar to a technique employed by Houze (1973). It is based on the assumption that convective cells have peak rainfall rates at least twice as high as the surrounding background rainfall rate. Data points in the reflectivity field that have rain rates twice as high as the average taken over the surrounding 400 km^2 of reflectivity are identified as the cores of con-

TABLE 1. Frequency distribution of particles in clusters A, B and C. The numbers indicate the percent of particles sampled for each cluster that fell into the corresponding size and shape categories. "None" means that not only were there no particles in this size-shape category found in the sample of images studied, but no particles of this type were found in any of the particle images associated with these penetrations. Small particles are <0.5 mm in diameter, medium ≥ 0.5 mm and <1.2 mm and large particles are ≥1.2 mm in diameter.

	Particle type								
	Cluster A			Cluster B			Cluster C		
	Small	Medium	Large	Small	Medium	Large	Small	Medium	Large
Columns	None	None	None	0.7	5.5	0.6	0.5	3.3	0.2
Branched crystals	None	None	None	0.3	5.1	3.0	0	0.2	0.9
Indeterminable	96.0	1.0	1.2	21.7	56.0	6.8	39.7	46.8	7.4
Nearly round	1.4	0.2	0.2	0	0.3	None	0.5	0.2	None

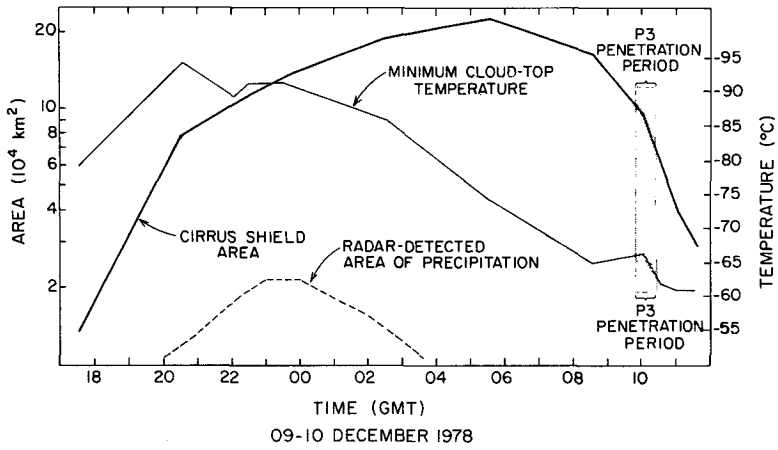

FIG. 17. Cirrus shield area, precipitation area and minimum cloud top temperature for cluster B. The area covered by the cirrus shield (thick curve) and the minimum cloud top temperature (thin curve) were determined from infrared satellite imagery. The area covered by precipitation from 2000 GMT 9 December to 0333 GMT 10 December 1978, is shown by the radar echo area (dashed curve) determined from the land-based radar. The shaded column indicates the period during which the P3 was in the cluster.

vective cells. For each core so identified, the surrounding 150 km^2 of area is considered "convective". In addition, any echo 40 dBZ (20 mm h^{-1}) or more in intensity is designated as convective whether or not it is considered convective by the above criterion. This rule is needed because occasionally an area of convection becomes so large and crowded with intense cells that the background rainfall rate becomes too large to be exceeded locally by a factor of 2. The inclusion of this 40 dBZ rule makes only a slight difference in the results of this case study.

Stratiform precipitation is identified as any precipitation not designated as convective by either of the above criteria. It is precipitation that is less than 40 dBZ in radar-echo intensity and generally lacking in horizontal variability. Areas of relatively weak cores, such as those with 21–30 dBZ intensity in the southwestern and southern portions of the echo pattern in Fig. 18e, were identified as convective by our procedures although vertical cross sections through these particular regions revealed a well defined radar bright band, indicating that this precipitation might be considered stratiform despite the horizontal variability within the regions. Radar-echo maps for times immediately preceding the Fig. 18e map indicated that the weak cells present in the south and southwest at 0001 GMT were the dying remnants of earlier more intense convection. Our technique did not consider these dying remnants as stratiform until they lost more of their horizontal variability. Hence, we believe that our partitioning method does not in general overestimate the areas covered by stratiform precipitation.

Our partitioning method suffers a minor limitation in dealing with small isolated patches of precipitation. Since it searches a reflectivity pattern for spatial maxima of rainfall rate, the technique cannot accurately classify as convective or stratiform patches of precipitation less than ~20 km (or 5 data points) in diameter. Consequently, both weak isolated convection and fractus of stratiform precipitation look identical. In treating isolated precipitation, we excluded echo-free air from the determination of background rainfall rate, and averaged only over areas with reflectivity 1 dBZ or greater. For isolated precipitation consisting of say 1 data point, the background rainfall rate was identical to the maximum value, hence the factor of 2 could never be exceeded. Therefore, the technique called patchy precipitation stratiform. This can be a source of error during the convective stage; for example, the arm of precipitation in Fig. 18b that extends out to sea northwest of the main cluster feature was classified as stratiform, even though it actually was convective. But in cluster B, most of the precipitation was connected in a single large mass, so that this error did not affect our primary results.

c. Time variation of convective and stratiform regions

The evolution of the internal structure of cluster B is revealed by examining the time variation of the convective and stratiform regions identified by the technique described in the preceding subsection. Consistent with the typical cloud cluster life cycle revealed by previous studies (see Section 1), the initial echo pattern (Fig. 18a) shows a group of convective cells with no evidence of stratiform precipitation. The cells were organized in a line parallel to the coastline, in the diurnally produced offshore convergence zone. During this early stage, cells increased in both number (Fig. 19a) and intensity (indicated by the decreasing

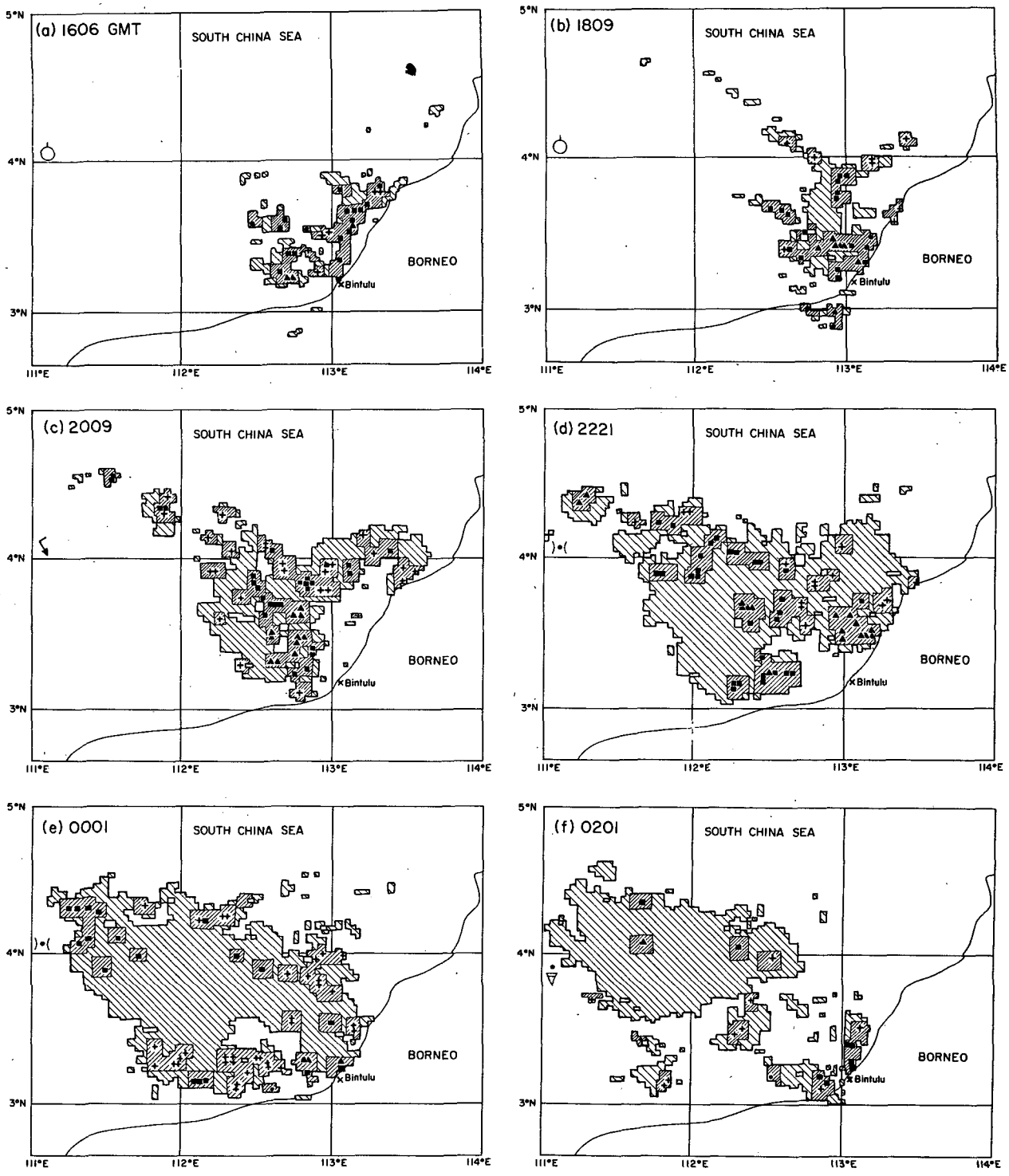

FIG. 18. Radar-echo patterns at 3 km in cluster B: (a) 1606 GMT (0006 LST); (b) 1809 GMT (0209 LST); (c) 2009 GMT (0409 LST); (d) 2221 GMT (0621 LST); (e) 0001 GMT (0801 LST); (f) 0201 GMT (1001 LST) 10 December 1978 [GMT times on the 9th except for (e) and (f)]. The radar was based at Bintulu, about 3.2°N, 113.1°E. The thin curve shows the northern coast of Borneo. Light shading is stratiform precipitation, heavy shading is convective. The dBZ values of objectively identified convective cores are indicated by dots (1–20 dBZ), crosses (21–30 dBZ), squares (31–40) dBZ and triangles (>40 dBZ). The symbols on the left side show the current weather reported by *Ak. Korolov*, located at 4°N, 111°E. This same weather data is included in Fig. 21.

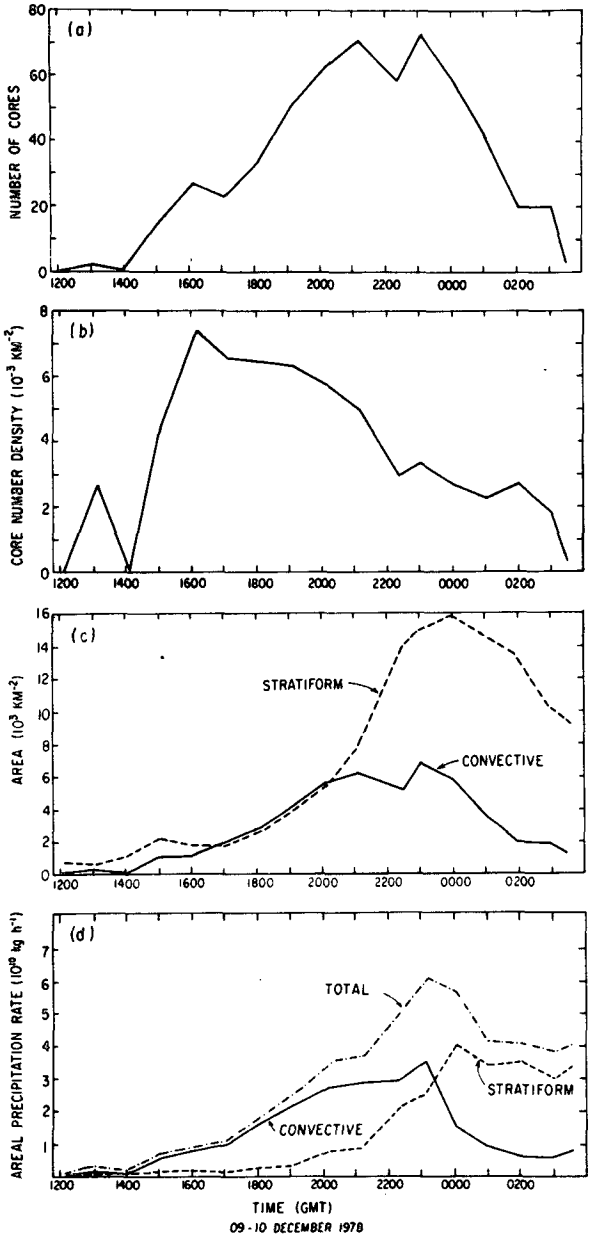

FIG. 19. (a) Number of convective cores in cluster B. (b) Number density of convective cores in cluster B, computed by dividing the values shown in (a) by the total area covered by precipitation at 3 km shown in (c). (c) Area covered by objectively determined stratiform (dashed curve) and convective precipitation (solid curve) at 3 km, defined by a 1 dBZ threshold. Part (d) shows area-integrated precipitation rate for cluster B at 3 km. The top (dot-dashed line) represents the sum of the convective (solid line) and stratiform (dashed line) components of precipitation.

minimum cloud top temperature in Fig. 17). The maximum number and intensity of cells were reached at about 0000 GMT, the same time the total area covered by precipitation (indicated by the radar-echo curve in Fig. 17) was greatest. However, the number density of cells (i.e., the number of cells per unit area of echo), shown in Fig. 19b, was maximum at the very beginning of the cluster (about 1600 GMT 9 December). At this time, an increasing proportion of the total rain area detected by radar was stratiform (light shading in Figs. 18b–e). The area of the stratiform precipitation is compared in Fig. 19c with the area covered by convective cells. The growth rate of the stratiform and convective areas were similar until about 2100 GMT, then the stratiform area expanded much more rapidly. This expansion during the later stages of development accounted for a proportionate increase in the area-integrated rainfall rate in the stratiform region (Fig. 19d). After 2333 GMT the area rainfall rate in the stratiform region exceeded that in the convective region. The area under the curves in Fig. 19d indicate that about 46% of the rain detected by radar in cluster B fell as stratiform rain. This proportion compares well with values of 30–50% reported for other tropical cloud clusters (Houze, 1977; Gamache and Houze, 1983; Houze and Rappaport, 1984; Leary, 1984).

d. Origin of the stratiform precipitation

As noted in Section 5b, some of the stratiform precipitation in cluster B appeared at locations that were previously convective but, where the cells weakened, became stratiform and blended into the background precipitation.

Figure 20 shows, however, that this process cannot have explained the development of all stratiform precipitation in the cluster. The rain area shown in Fig. 20 is the union of the total rain areas seen at each of the individual times in Fig. 18. In addition, the objectively determined convective-core positions shown in the panels of Fig. 18 have been reproduced in Fig. 20, with each dot representing one core. Between 3.0 and 4.0°N, and between 111.5 and 112.2°E there was a region (outlined by the dashed curve) in which no convective cores were detected at the six times, but in which stratiform rain developed and persisted for about 4 h. In this convectively dormant area, the stratiform precipitation was not the residue of cells previously active in this area. Instead, this stratiform precipitation must have resulted either as blowoff of hydrometeors from convective cells located in other areas, as a result of a mesoscale updraft in the cloud deck, or as a combination of these effects. Both probably contributed in the case of cluster B. The easterly middle and upper level tropospheric winds seen in Figs. 3 and 4 could have advected hydrometeors from the tops of cells in the eastern part of B into the core-free area. In addition, evidence of mesoscale updraft motion in the cloud deck of cluster B is found in the microphysical data (see Section 5f), and the magnitude of this mesoscale updraft has been determined in diagnostic studies of the ship soundings (Johnson, 1982) and of the ice budget of the stratiform cloud deck (Churchill and Houze, 1984)..

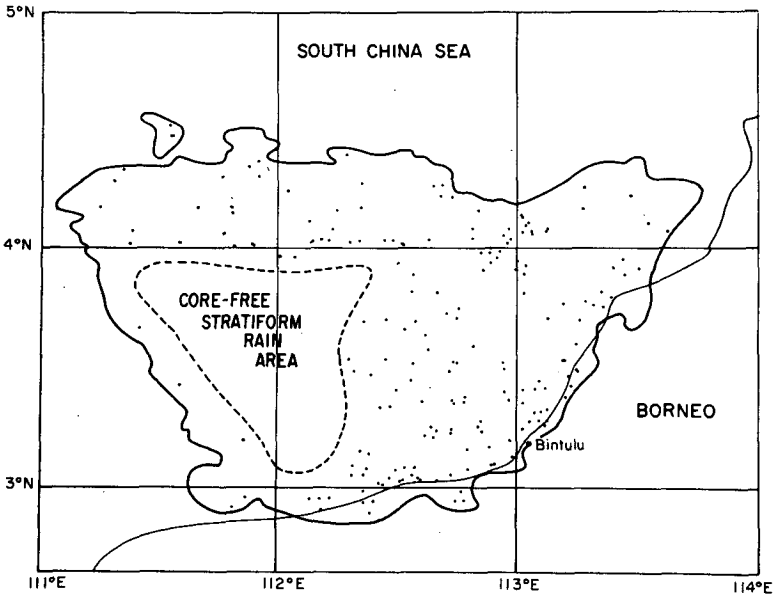

FIG. 20. Composite of 3 km level radar-echo pattern. The thick curve denotes the union of the areas of precipitation shown in Fig. 18. The dots represent the objectively located convective cores which were indicated by crosses in Fig. 18. The dashed line highlights a region where stratiform rain fell for about 4 h and in which no objectively located cores were present.

e. The pattern of convection

When cluster B became evident in satellite imagery at 1733 GMT (Fig. 6), the radar echo pattern consisted almost entirely of convective cells (Fig. 18a). Throughout the remainder of the cluster's lifetime, intense cores (over 30 dBZ) were found in the greatest numbers on the southeast side of the echo near, and parallel to, the coastline (Figs. 18b–f). Evidently, these cores were forming in response to convergence of the land breeze with winds over the sea. They became less numerous after sunrise (Figs. 18e and f) and disappeared by midday, when the land breeze had been replaced by a sea breeze.

In addition to the cores evidently forced by land-breeze convergence near the coast, the cluster developed convection along its northern and northwestern boundaries. Throughout the day, the northwestern boundary of the precipitation area progressed northwestward (note the northwestern extent of the echo region in the successive panels of Fig. 18). The northwest edge of the echo moved out of radar range after 0000 GMT. However, at 0200 GMT, heavy rainshowers were reported at *Ak. Korolov* (see reports in Figs. 18f and 21), which was located just beyond the boundary of the radar area.[5]

The pattern of convection, composed of cores forced by the land-breeze convergence along the coast together with the cores to the northwest gave the appearance of a broken line or elliptical ring of convective cells distributed around a central broad region of stratiform precipitation at 0001 GMT (Fig. 18e). Since the convection to the northwest was moving northwestward while the cores to the southeast remained tied spatially to the region just off the coast, the broken ellipse of convective cells evident at 0001 GMT was expanding along a northwest–southeast axis.

By 0201 GMT, the total precipitation area had broken into two distinct parts, a large trailing stratiform region associated with the convective cores which had moved northwestward out of radar range and the land-breeze forced cores remaining along the coast near Bintulu.

f. The mesoscale downdraft

The typical vertical motion profile associated with the stratiform region of a cloud cluster consists of a mesoscale updraft in the middle to upper level cloud deck, with mesoscale subsidence below the 4–5 km level cloud base (Gamache and Houze, 1982; Johnson, 1982; Houze and Rappaport, 1984). It was noted in a preceding discussion (Section 5b) that a mesoscale updraft evidently contributed to the development of stratiform precipitation in the central region of B. At the same time, the mesoscale downdraft at lower levels apparently suppressed the development of deep convection in this region.

Evidence of the mesoscale downdraft can be seen in soundings from the ship *Ak. Korolov* and from P3

[5] The ring of new cloud cluster activity that was evident around cluster B in the satellite imagery discussed in Section 3 (Figs. 6g–l) may have been a further manifestation of the tendency for deep convective cells to form in an ever-increasing arc around cluster B.

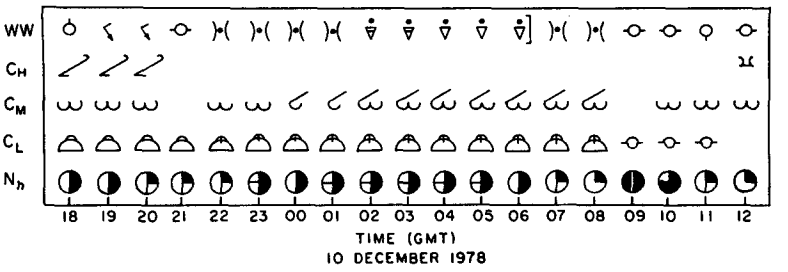

FIG. 21. Clouds and weather beneath cluster B reported by the ship *Ak. Korolov*. The top row shows the current weather (WW), the second shows the high clouds (C_H), the third shows the middle clouds (C_M), the fourth shows the low clouds (C_L) and the bottom row shows the fraction of sky covered by low and middle level clouds (N_h).

and Electra dropwindsondes obtained between 0800 and 1000 GMT. Most of these soundings are shown in Fig. 22, and the positions of the ship, dropwindsondes and the aircraft tracks through cluster B are indicated in Fig. 23. The P3 airborne radar data (not shown) indicated no convective precipitation, although very weak stratiform precipitation (approximately 15 dBZ) existed in the immediate vicinity of the aircraft along the shaded portions of the flight track. (Since this weak echo was below minimum detectable intensity at ranges of 10–15 km, its full horizontal extent could not be determined.) Surface weather observations indicated, however, that little of this precipitation was reaching the surface and that the precipitation was ending at *Ak. Korolov* during the 0800–1000 GMT period (Fig. 21). From Fig. 17 it is evident moreover, that the P3 penetration occurred very late in the lifetime of the cluster, when the area of the cloud shield was decreasing and the minimum cloud top temperature was increasing. Thus, the two P3 dropwindsondes (Figs. 22c and f), the two Electra dropwindsondes (not shown) and the two *Ak. Korolov* soundings obtained along the aircraft track between 0800 and 1000 GMT (Figs. 22d and e) sampled a very old, decaying portion of the stratiform region of cluster B. For comparison, Figs. 22a and b contain the WMONEX mean and 0000 GMT 10 December 1978 soundings for *Ak. Korolov*. The latter was obtained just before cluster B moved over the ship (Figs. 6 and 18) and it strongly resembled the mean sounding (except for the possibly spurious layer of low wet-bulb potential temperature at 500–550 mb).

The soundings in the decaying stratiform region (Figs. 22c–f) all showed marked deviation from the main structure seen in Figs. 22a and b. This deviation was evidently produced by an unsaturated downdraft below the stratiform cloud base of cluster B. Each of these soundings was a typical mesoscale downdraft sounding (Zipser, 1977), characterized by a low-level subsidence inversion with the dew point depression decreasing with height up to the base of the stratiform cloud approximately 500 mb. The roughly constant wet-bulb potential temperature value of 294 K in the unsaturated layer between cloud base and inversion indicated that this air was subsiding from about the 500–600 mb level (cf. Figs. 22a and b). Since each sounding obtained by the Electra and the P3 in cluster B indicated this subsidence, it is evident that the downdraft was a mesoscale feature. The height of the inversion, i.e., the level to which the mesoscale downdraft descended, varied from 800 (Figs. 22c and f) to about 950 mb (Figs. 22d and e). Differences in the height of the inversion, however, could be an artifact of comparing dropwindsondes with rawinsondes. The layer of air below the inversion in Figs. 22c–f was well mixed with high wet bulb potential temperature (297–299 K) at the surface, characteristic of the undisturbed air mass (Figs. 22a and b).

The effect of mesoscale subsidence is also seen in a photograph obtained when the P3 left the cloud deck of cluster B (Fig. 24). Beneath the altostratus ceiling was a suppressed region with small cumulus over the ocean, consistent with cloud reports from *Ak. Korolov* (Fig. 21). Low-level cumulus, illuminated by sunshine (but not easily seen in the black and white reproduction) near the horizon in Fig. 24, indicated that the edge of the suppressed area was positioned beyond the periphery of the cloud deck.

g. Convective-scale downdrafts

In addition to the mesoscale stratiform subsidence, which suppressed convective development in the central region of B, convective-scale downdrafts were undoubtedly associated with the individual convective cores in the cluster. [See Zipser (1977) and Houze (1977) for a discussion of the differences between mesoscale subsidence in stratiform regions and convective-scale downdrafts.] Evidence of convective downdraft outflows in B was noted by observers on board the NCAR Electra as the aircraft approached cluster B. Towering cumulus was observed northwest of the Electra at 0745 GMT (see Fig. 23), while suppressed areas with stratocumulus were noted to the southeast.

h. Microphysical observations

Although the P3 penetration of cluster B occurred during the late decaying stage of the cluster, the cloud

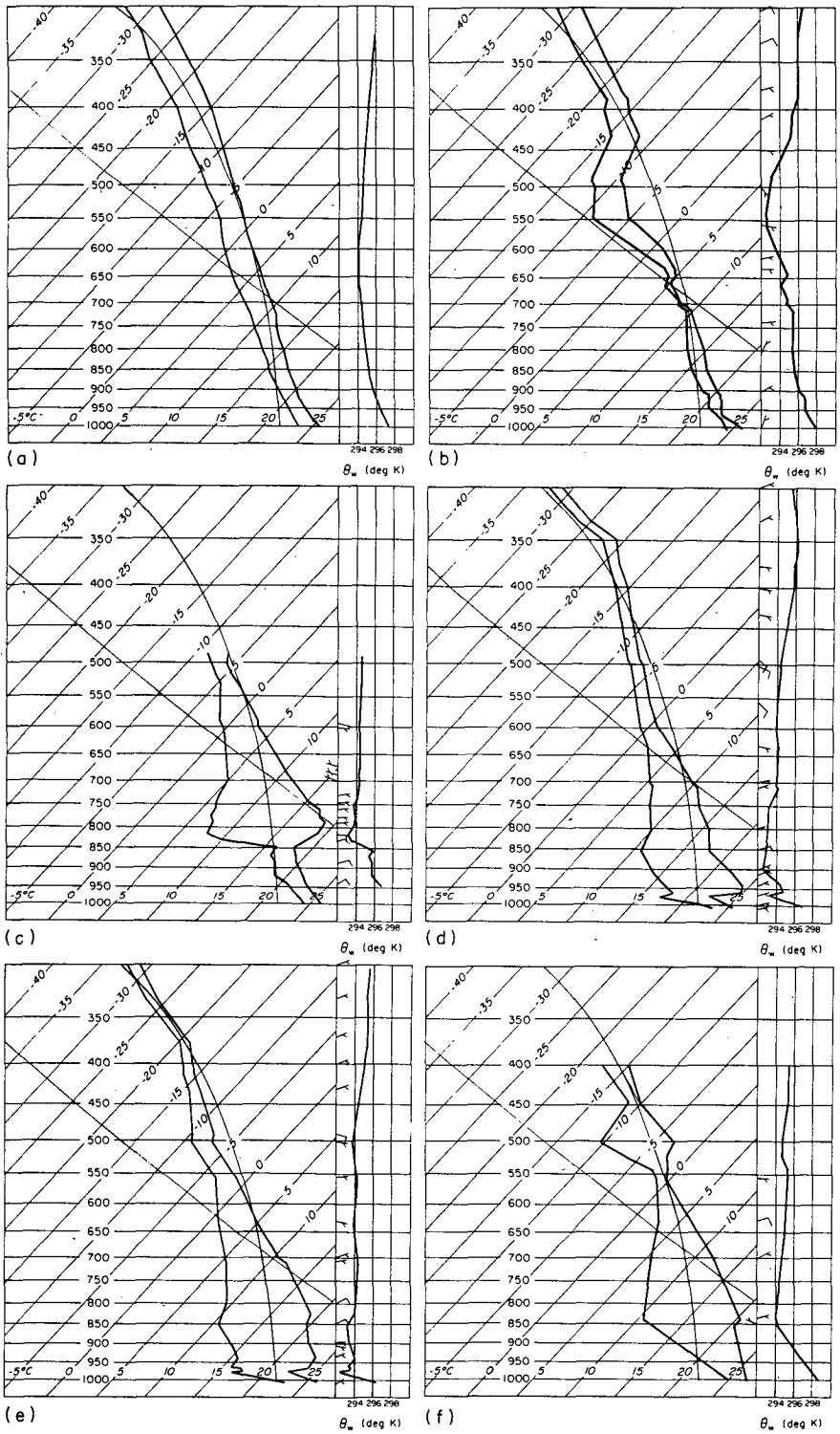

FIG. 22. Environmental and mean soundings for cluster B: (a) is the mean Winter MONEX sounding for *Ak. Korolov* (provided by R. H. Johnson); (b) *Ak. Korolov* rawinsonde for 0000 GMT 10 December 1978; (c) P3 dropwindsonde at 0940 GMT released at 4.33°N, 111.35°E; (d) *Ak. Korolov* 0800 GMT; (e) *Ak. Korolov* rawinsonde for 0900 GMT; and (f) P3 dropwindsonde at 1000 GMT, released at 3.49°N, 109.93°E. Solid curves show temperature, dew point and wet bulb equivalent potential temperature (θ_w). Barbs show wind speed (one full barb 5 m s^{-1}) and direction.

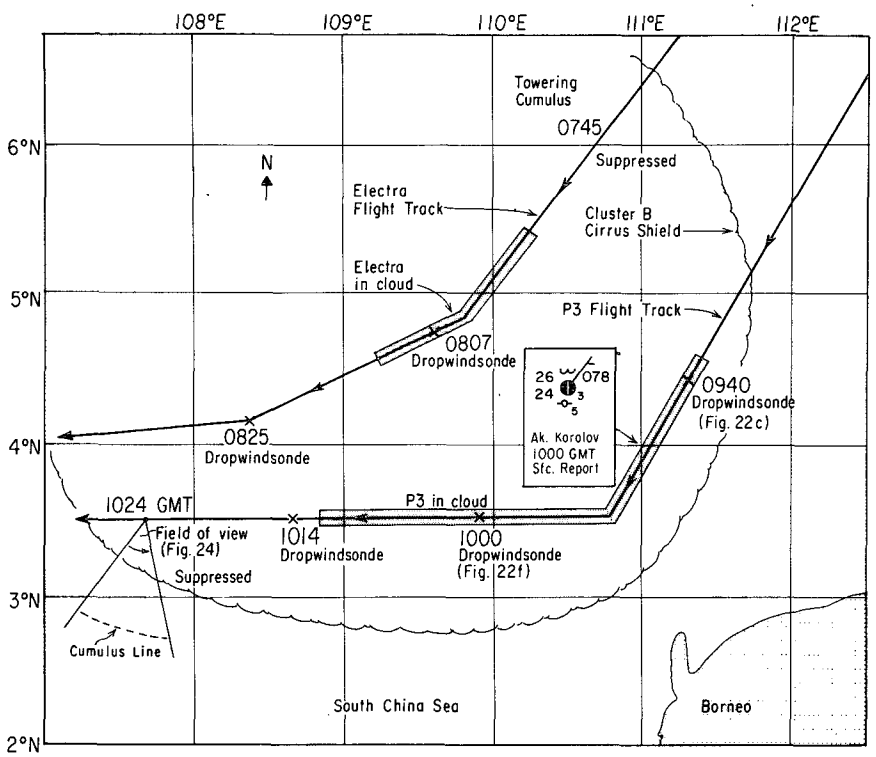

FIG. 23. Summary of cluster B showing flight tracks of the P3 and Electra, dropwindsonde locations (crosses), cirrus shield perimeter, cloud line location and surface report of *Ak. Korolov* and vantage point for a photograph. Figure numbers refer to further descriptions of the data. The shaded boxes along the flight tracks indicate where the aircraft were in cloud.

appeared quite dense to observers on the aircraft and precipitation-size ice particles were detected by the PMS cloud probe. These particles produced the weak, 15 dBZ radar echo detected along the flight track (Fig. 23). Table 1 summarizes the types and sizes of the ice particles encountered. Comparison of clusters A and B points out a striking difference between the samples of ice particles obtained in them. In A, the only identifiable ice particles were nearly round (i.e., graupel or other heavily rimed particles), whereas in B, (with the exception of two occurrences of nearly round particles near the end of the penetration) the only identifiable types were columns and branched crystals (i.e., vapor grown crystals). The difference between the determinable particles in the two samples is attributable to sampling cluster A in convective cells while sampling cluster B in its stratiform cloud deck.

A striking difference between the two samples is also seen in the size distribution of indeterminable particles. Although the vast majority of the particles were indeterminable in both A (85%) and B (98%), medium and large indeterminable particles accounted for 63% of the particles in B, compared to 2% in A. This difference in size distributions between A and B was probably associated with a qualitative difference in the particles. We have already suggested that the indeterminable particles in A were probably small rimed particles, since the identifiable particles were all rimed. By similar reasoning, we suggest that since the identifiable particles in B were almost exclusively vapor grown crystals, it is likely that the indeterminable particles in B were also vapor grown crystals. Many of these indeterminable particles, especially in the middle and large size categories (i.e., greater than or equal to 0.6 mm in diameter) had straight edges and sharp corners, further suggesting that they were vapor grown rather than rimed. Since the liquid water content at flight level in cluster B was below the minimum detectable threshold of the Johnson-Williams device, riming was unlikely. Many of the indeterminable images in B may have been produced by broken or aggregated crystals, while others may have resulted from passage of ice particles through several temperature–humidity regimes. We suggest that the predominant ice particle growth modes above the 0°C level in the stratiform region of this cluster were vapor deposition and aggregation.

Generally, crystals with more complex structure and branching grow at higher ice supersaturations (Hobbs, 1974, p. 660). The branched crystals in cluster B appear

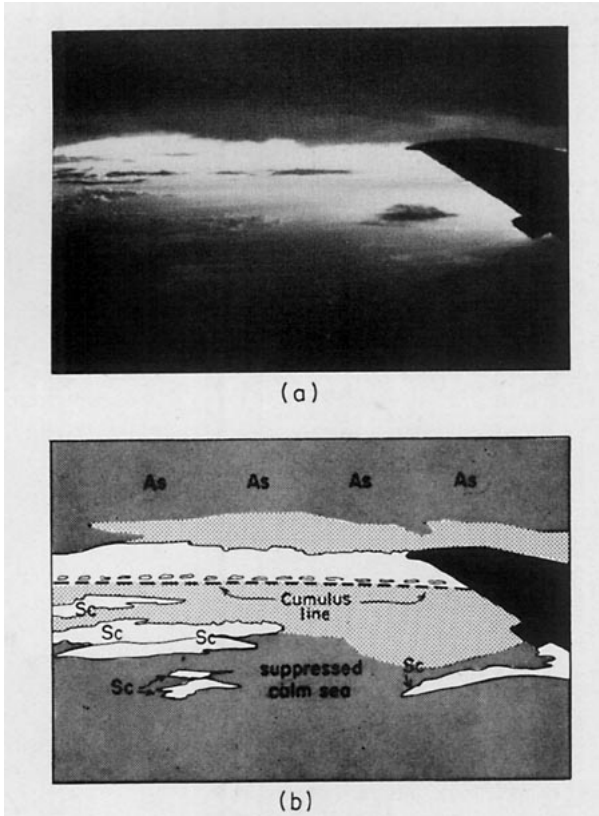

FIG. 24. (a) Photograph of the underside of the cloud deck of cluster B, taken at 1024 GMT (1824 LST) 10 December 1978 at 3.5°N, 107.7°E, looking south out of the left side of the P3. Aircraft altitude was 7.8 km. The shadow of a cloud line on the sea surface can be seen in the distance in the color original of this picture. Photo by R. A. Houze, Jr. (b) Nephananalysis shows the ceiling of the cloud deck of cluster B, with calm seas and suppressed cloudiness near the surface, and a weak line of cumulus in the distance (dashed line).

to have been of a type (apparently sideplanes, or some similar branched structures, see the Appendix) that grow at humidities approaching water saturation at temperatures of −17 to −25°C. Since the flight-level temperature was between −16 and −17°C, these crystals must have grown above flight level in cluster B's stratiform cloud deck and drifted down to flight level in an environment possessing upward air motion strong enough to maintain supersaturation with respect to ice but weak enough to allow the ice particles (which have terminal velocities of about 1–2 m s^{-1}) to fall. This result is consistent with other observational evidence regarding vertical air motions. Vertical wind speeds measured aboard the P3 never exceeded the noise level anywhere along the 350 km flight track through B, while vertical motions of tens of centimeters per second are deduced from the ice budget of cluster B by Churchill and Houze (1984) and from the ship sounding data for B by Johnson (1982). Since ice particles of similar character, uniform weak radar echo and vertical air motions of similar magnitude were found all along the 350 km distance of the P3's track through B, it is evident that the vertical motions there constituted a *mesoscale* updraft at and above the level of the aircraft.

Figure 25 shows the variation of the particle concentration detected by the PMS cloud probe along the flight path through cluster B. The total concentration of particles was generally between 1 and 10 per liter, two orders of magnitude lower than the values that predominated in the convective cells of cluster A (cf. Fig. 16). This persistently lower concentration of particles was consistent with the samples being taken in an aged stratiform portion of the cluster.

The concentration of particles by type shown in Fig. 25 was estimated by multiplying the total concentration by the fractional portion of each one minute sample associated with each particle type. The total concentration was consistently dominated by the indeterminable particles. Identifiable particles (columns, branched crystals, nearly round) were generally present in concentrations of less than 1 per liter. Variations in the identifiable particle concentrations showed that the internal structure of the stratiform cloud was not perfectly uniform. The aircraft passed in and out of small mesoscale regions (30–100 km across) of enhanced concentrations of columns and branched crystals. This nonuniformity could be associated with convective overturning within the cloud deck and is also consistent with the notion of cell dissipation as a

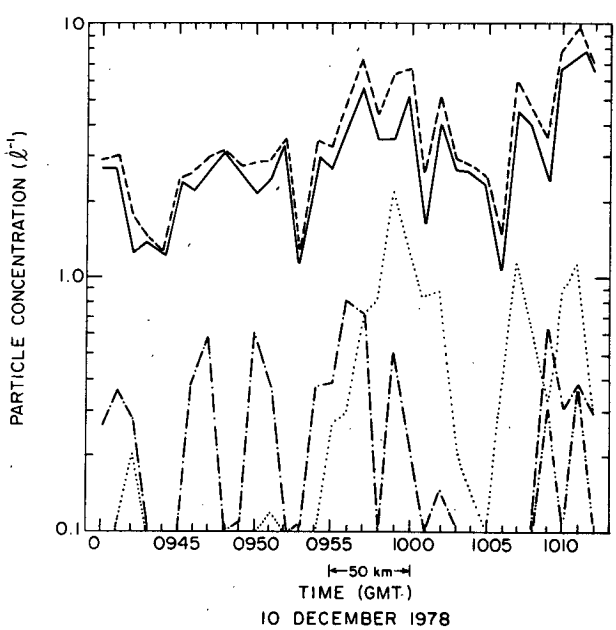

FIG. 25. Ice particle concentrations (per liter) in cluster B. The total concentration of particles (dashed line) is the sum of the concentrations for indeterminable (solid line), columns (dot-dashed line), branched crystals (dotted line) and nearly round particles (dash-double dot line). Values are one-minute averages.

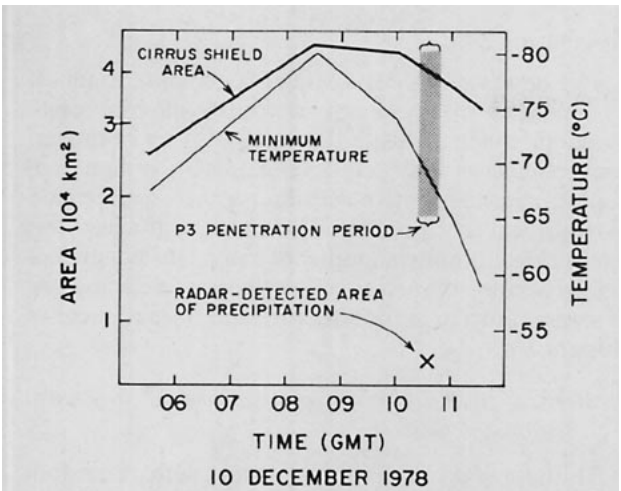

FIG. 26. Cirrus shield area, precipitation area and minimum cloud top temperature for cluster C. The areas covered by the cirrus shield (thick curve) and the minimum cloud top temperature (thin curve) were determined from infrared satellite imagery. The area covered by precipitation (indicated by the cross) was determined from the P3's lower fuselage radar. The shaded column indicates the period during which the P3 was in the cluster.

mechanism for stratiform cloud formation. The largest of these regions was 100 km wide in the central portion of the penetration (0954–1005 GMT), where the peak concentration was 2 per liter. This region was probably where the mesoscale updraft was strongest, producing higher supersaturation and thus, more complex crystals above flight level. The only region where nearly round particles were noted on the flight was near the end of the penetration (1008–1012 GMT) and they were accompanied by columns and branched crystals.

6. Cloud cluster C

a. Satellite and radar data

The P3 entered cluster C at 1033 GMT when the cluster was in a late stage of development (Fig. 26). Two hours had passed since the minimum cloud top temperature and maximum areal coverage of the cluster occurred. Nevertheless, the precipitation area detected by the airborne radar during the penetration (Fig. 27) exhibited the structure of a mature cloud cluster. The echo pattern, which resembled that seen in cluster A (Section 4), showed several convective cells (characterized by strong horizontal gradients over small areas) on the eastern edge (3.5°N, 107.4°E), while widespread stratiform precipitation, characterized by low horizontal gradients of reflectivity, covered most of the 8.0×10^3 km^2 area of the echo pattern.

b. Microphysical observations

The flight track in Fig. 27 shows that after passing through the convective region, the P3 flew through stratiform echo for about 200 km. The stratiform radar reflectivity, which was 20–27 dBZ, was considerably denser than the 15 dBZ stratiform region sampled in cluster B (Section 5f). The ice particle concentrations observed with the PMS cloud probe between 1031 and 1039 GMT (Fig. 28) confirmed this difference. Concentrations in cluster C were around 40 per liter, about one order of magnitude greater than those in B (cf. Fig. 25). After 1039 GMT the aircraft flew through a weaker stratiform echo (less than 20 dBZ in intensity), and the total particle concentration dropped by an order of magnitude to values similar to those of cluster B.

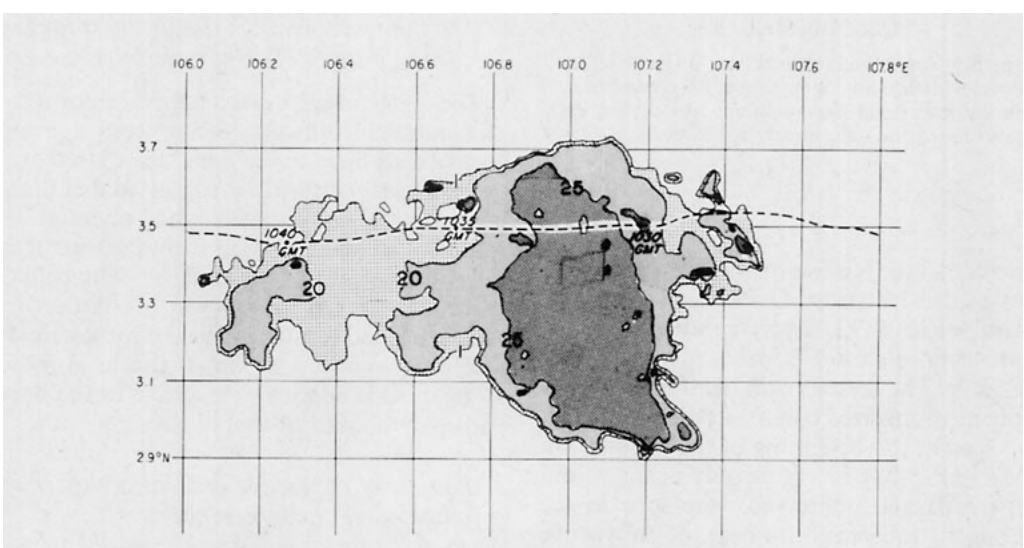

FIG. 27. Radar depiction of cluster C. The dashed line indicates the flight track of the P3 through cluster C. Contours of radar reflectivity are for 1, 20, 25 and 30 dBZ. The area of this pattern (8.0×10^3 km^2) is indicated in Fig. 26 by the cross.

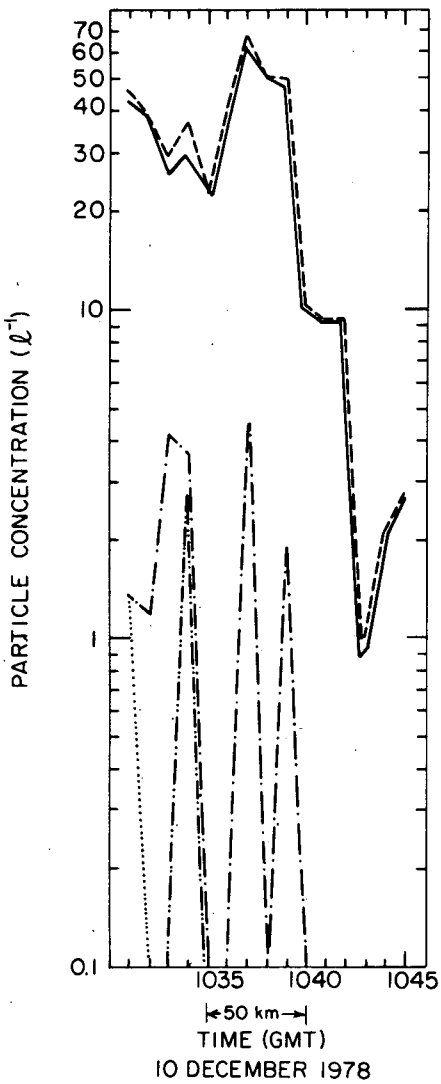

FIG. 28. Ice particle concentrations in cluster C. The total concentration of particles (dashed line) is the sum of the concentrations for indiscernible particles (solid line), columns (dot-dashed line), branched crystals (dotted line) and nearly round particles (dash-double dot line).

Table 1 shows that the relative frequency distribution of particles sampled in cluster C was very similar to that of B. Most particles (93.9%) were indeterminable, and as was the case in cluster B, more than half were medium and large. The crystals with identifiable habits were primarily medium-sized columns. A few branched crystals were seen at the beginning of the penetration (at 1031 GMT in Fig. 28). Since the only nearly round (i.e., rimed) ice particles observed were seen in the region of stronger stratiform echo near the convective cells on the eastern edge of C, we suggest that this region had remnants of recently active cells that were becoming stratiform.

7. Conclusions

The observations of WMONEX cloud clusters on 10 December 1978 generally conform to the conceptual model in which a cluster begins as a group of intense convective cells and then develops into a system containing both convective cells and a mesoscale region of stratiform precipitation. These observations on this day enrich our understanding of cloud clusters by providing detailed observations, not heretofore available, of several aspects of the structure and development of clusters.

a. Vertical motions in the convective and stratiform regions of clusters

The data of this study are consistent with other studies of vertical motions in convective cells and the stratiform regions of tropical cloud clusters. The aircraft penetrations of cells in cluster A showed updrafts similar in intensity to those studied by LeMone and Zipser (1980). Soundings in the stratiform region of cluster B showed evidence of unsaturated mesoscale downdraft motion in the middle to lower troposphere, below the base of the stratiform cloud, and ice particle habits observed in stratiform regions indicated a mesoscale updraft at middle to upper levels. The configuration in which the mesoscale updraft in the stratiform cloud lies above the unsaturated mesoscale downdraft below cloud base is consistent with the cloud cluster vertical motion profiles determined from sounding data in other studies (Gamache and Houze, 1982; Johnson, 1982; Houze and Rappaport, 1984). In a subsequent paper (Churchill and Houze, 1984), the magnitude of the mesoscale updraft in the stratiform cloud of cluster B is deduced from the ice budget of the cloud.

b. Mechanisms by which the stratiform region evolves from a group of convective cells

The mechanisms by which the stratiform component of a mesoscale cluster evolves from a group of convective cells have never been clear. Houze (1977) and Leary and Houze (1979a) suggested that the stratiform precipitation is initiated and maintained by the spreading of hydrometeors from the tops of convective cells by divergent winds aloft, by older cells dying and becoming stratiform, or by condensation in the mesoscale updraft located above the mesoscale downdraft. The radar-echo evolution in cluster B indicates that *all* of these processes were active in the development and maintenance of that cluster.

c. Pattern of convective cells in a cluster affected by land–breeze convergence

Over the open ocean, the deep convection in tropical cloud clusters often occurs in propagating lines of cells, with the stratiform regions of the clusters trailing the

lines. These convective lines move rapidly in the case of squall lines (e.g., Zipser, 1969, 1977; Houze, 1977) and more slowly in non-squall clusters (e.g., Leary and Houze, 1979a; Zipser *et al.,* 1981). The large cloud cluster B examined in detail in this study occurred near a coastline, rather than far out to sea. The convective cells in B tended to occur in a broken line around the periphery of the stratiform region. The convection on the seaward side of the cluster propagated (moving ever farther out to sea) in a manner somewhat similar to the oceanic clusters referred to above. The convective cells on the landward side of the cluster, however, were evidently forced by land-breeze convergence and consequently remained in the same general area—just off the Borneo coast, where the convergence was occurring—throughout the life of the cluster.

d. Triggering of new convection by downdraft outflows

It has often been noted that new cloud clusters tend to form near the edges of old cloud clusters. This fact is typically attributed to intensified convergence at the edges of horizontally expanding pools of dense convective downdraft air spreading out at the surface from older clusters, though other explanations may also be offered (see Section E1A of Houze and Betts, 1981). In this study, new clusters were observed to form around cluster B during its later stages, and observations obtained in zones between cluster B and clusters A, C and I indicate that downdraft outflows were active in these regions and thus suggest that such outflows may have been involved in triggering the new clusters around B. These observations, however, are circumstantial and more definitive measurements regarding the effect of old clusters on new ones are needed in future studies.

e. Ice particle structures and concentrations in convective and stratiform regions

Leary and Houze (1979b) inferred structures of ice particles in the cloud decks of tropical cloud clusters from the vertical distribution of radar reflectivity and observed size distributions of raindrops falling from the clouds. However, the microphysical structure in tropical cloud clusters above the 0°C level has not been deduced from direct observations of the ice particles prior to the present study. Aboard the P3 aircraft, samples of ice particles in the 0.1–1.6 mm size ranges were obtained near the −17°C level in both the convective cells and stratiform regions of clusters.

Ice particles in convective cells were found in concentrations of 100–400 per liter. The dominant identifiable particle type was nearly round graupel, indicating that the primary growth mode was riming. This growth mode was consistent with the updraft speeds of 4–17 m s^{-1} encountered by the aircraft. Nearly all of the particle characteristics need to be explored by flights at more than one level.

The ice particles in stratiform regions had lower concentrations than in convective cells and the predominant growth modes appeared to be vapor deposition and aggregation rather than riming. Nonuniformity in the stratiform region was indicated by variation in the dominant crystal habits over horizontal distances of 10–100 km. Occasionally particles with rimed characteristics were mixed in with the vapor-grown particles in propinquity to active convective cells. In weak stratiform areas (radar reflectivity factor approximately 15 dBZ) particle concentrations were 1–10 per liter, while in moderate and strong stratiform areas (20–27 dBZ) particle concentrations were 20–70 per liter.

The marked difference between the ice particle characteristics of convective cells and stratiform regions seen in this study may be typical of tropical cloud clusters. More clusters should be examined to assess the generality of our results and the work should be extended to include the vertical distribution of particle characteristics in each type of region.

Acknowledgments. This work was aided by many people who provided data or assisted the data reduction and analyses. We especially thank B. Auvine, A. Biswas, S. G. Geotis, P. H. Herzegh, R. H. Johnson, F. D. Marks, D. W. Martin and C. Warner. Typing and drafting were performed by C. Arthur and K. Moore. This research was supported by the National Science Foundation Grant ATM80-17327 and by the National Center for Atmospheric Research through its Scientific Computing Division.

APPENDIX

Analysis of Two-Dimensional Ice Particle Images

The primary microphysical data used in this study are the two-dimensional particle images obtained with the PMS probe mentioned in Section 2. At flight level (7.8 km), the air temperature was about −17°C, and all the particles encountered appeared to be ice. Some examples of ice particle images reconstructed by computer and recorded on microfilm are shown in Fig. A1. The images are shaded in the vertical columns of the figure. The size of an individual particle may be estimated by comparing its diameter with the 1.6 mm width of the column. Either an "A" or an "R" is found under each image. The "A" means that the above image was acceptable; that is, a complete particle was detected by the probe and properly recorded on tape. The "R" indicates that the image as a "reject". The label immediately to the right cites one of several reasons for the rejection: If only a fraction of a cloud particle passed over the array of photodiodes in the

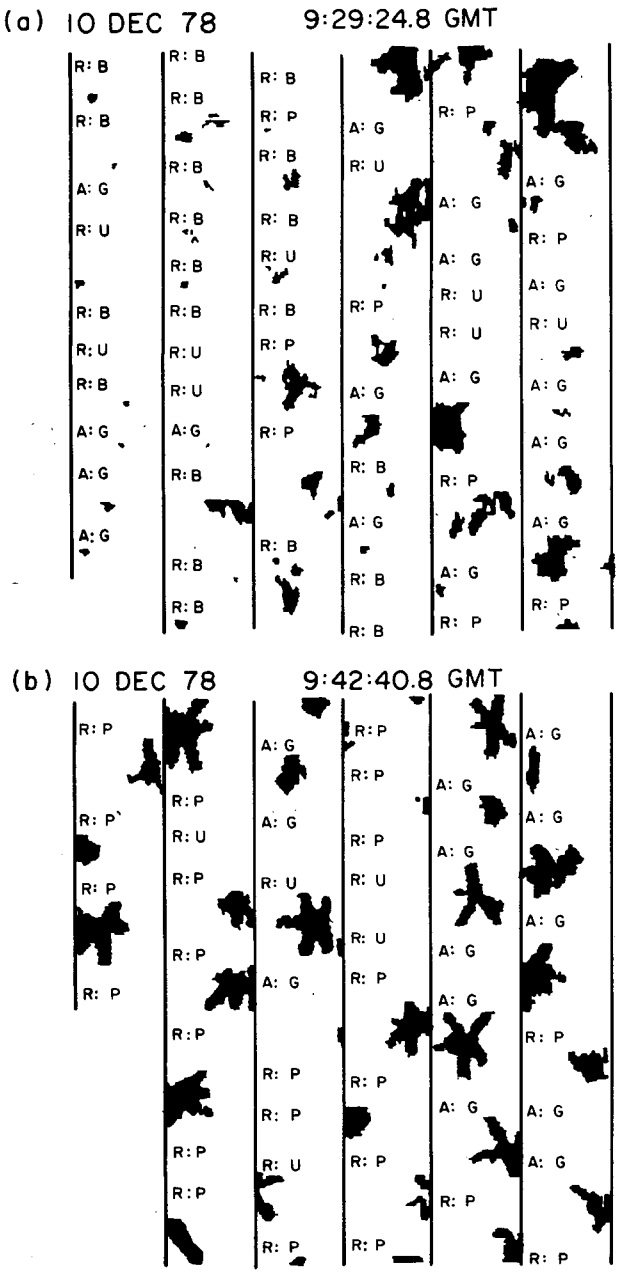

FIG. A1. (a) Sample of the microfilm output from the Knollenberg cloud probe. Included in this frame are examples of good (G), bad time (B), partial (P) and undersize (U) images. (b) Sample of sideplane images obtained by the P3 in cloud cluster B.

Knollenberg probe it is labeled *part image;* if a particle was too small to be adequately resolved by the probe it is labeled *undersize;* if the data were not properly recorded on tape *bad time* is indicated; if a particle was so large it overlapped the width of the photodiode array it is labeled *oversize.* Fig. A1 shows examples of good, partial, undersize and bad-time images.

The word *frame* is used to refer to the collection of particle images identified by a common time, such as the entirety of Fig. A1(a) or (b). Up to 30 frames were recorded on microfilm for each minute that the aircraft was in cloud.

Statistics were tallied to study the frequency of occurrence of ice particles, classified by size and shape, for each of the three cloud clusters penetrated by the P3 on 10 December 1978. A sample of images was obtained by scanning each frame from top to bottom and right to left until either a good image (as defined above) or a partial image that was at least two-thirds of a column wide was encountered. Then this image was entered into the sample. For example, the top right image in Fig. A1(a) is the first good image in that frame. Proceeding in this manner from frame to frame resulted in the accumulation of a sample of about 30 images for each minute of in-cloud flight.

The particle sample thus obtained was divided into *small, medium* and *large,* corresponding respectively to particles the maximum width of which were less than one-third of the 1.6 mm width of a column (less than 0.5 mm in width), at least one-third the width of the column (greater than or equal to 0.5 mm) but less than two thirds the width (less than 1.2 mm), and two thirds the width or larger (greater than or equal to 1.2 mm).

The ice particle sample was further divided into four categories of shape: *columns, branched crystals, nearly round* and *indeterminable.* Examples of images in each size and shape category obtained on 10 December (in clusters A, B and C) are shown in Fig. A2. The branched crystals (seen only in clusters B and C) appeared to be primarily sideplanes (Hobbs, 1974, pp. 656 and 660) whose three-dimensional habits produce planar shadows with four or five visible branches separated by unequal angles (Fig. A1b). Nearly round particles (seen in cluster A) were frozen drops, graupel, small hail or other ice particles producing nearly circular images. Particles whose habits could not be identified from their two-dimensional shadows were classified as indeterminable. These particles probably included aggregates of crystals, complex-growth structures produced as particles moved from one temperature–humidity regime to another and particles whose shapes were partially obscured by riming or complicated by other factors.

Because of the orientations in space that particles assume as they pass through a Knollenberg probe, the size and shape of asymmetric particles may be misclassified. For example, the thin edge of a dendrite might appear as a column or needle, or viewed from the end, a column might appear as a nearly round particle. Although such misclassifications may be a source of error in the size–shape distributions discussed in this study, we feel that the results are at least qualitatively accurate.

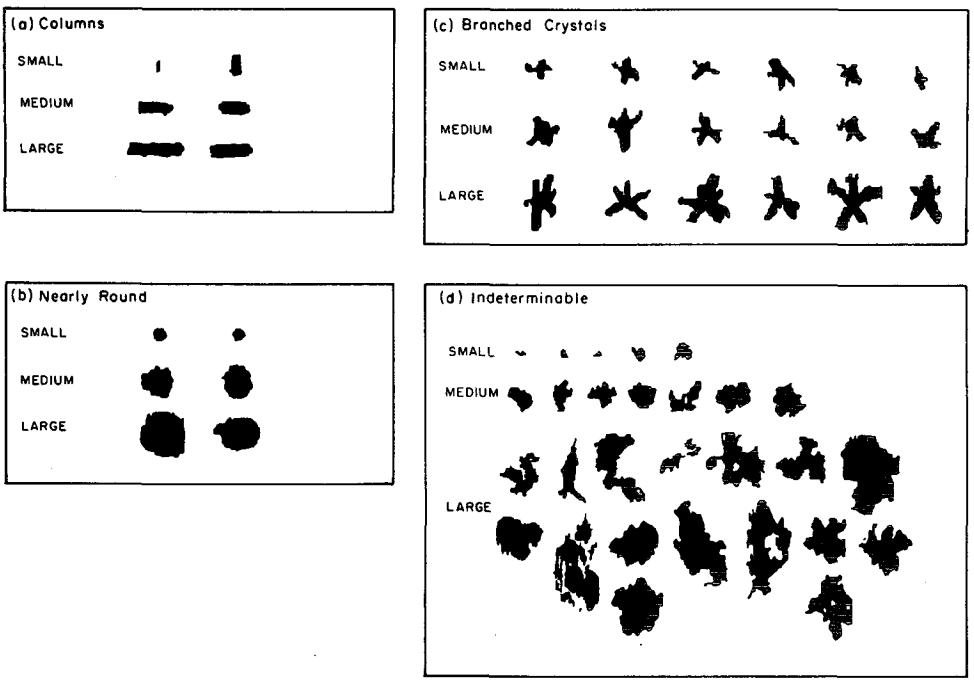

FIG. A2. Examples of ice particle habits and sizes. The different habits of ice particles encountered in the penetrations of 10 December 1978 are illustrated by a selection of images for each particle type and size: (a) columns, (b) nearly round particles, (c) branched crystals and (d) indeterminable particles. The size categories and particle types are defined in the text.

REFERENCES

Arkell, R., and M. Hudlow, 1977: *GATE International Meteorological Radar Atlas.* Environmental Data Service, NOAA Government Printing Office, 222 pp. [NTIS P3-277 233/3G1e].

Austin, P. M., and S. G. Geotis, 1979: Raindrop sizes and related parameters for GATE. *J. Appl. Meteor.*, **18,** 569–575.

Cannon, T. W., 1976: Imaging devices. *Atmos. Technol.*, **8,** 32–37.

Chang, C.-P., and K. M. Lau, 1980: Northeasterly cold surges and near equatorial disturbances over the Winter MONEX area during December 1974. Part II: Planetary-scale aspects. *Mon. Wea. Rev.*, **108,** 298–312.

——, J. E. Erickson and K. M. Lau, 1979: Northeasterly cold surges and near-equatorial disturbances over the Winter MONEX area during December 1974. Part I: Synoptic aspects. *Mon. Wea. Rev.*, **107,** 812–829.

——, B. K. Cheang and G. T. Chen, 1981: *Regional Synoptic Analysis during Phase I of Winter MONEX.* Department of Meteorology, Naval Post-graduate School, Monterey, CA 93940, 285 pp.

Churchill, D. D., and R. A. Houze, Jr., 1984: Mesoscale updraft magnitude and cloud-ice content deduced from the ice budget of the stratiform region of a tropical cloud cluster. *J. Atmos. Sci.*, **41** (in press).

Gamache, J. F., and R. A. Houze, Jr., 1982: Mesoscale air motions associated with a tropical squall line. *Mon. Wea. Rev.*, **110,** 118–135.

——, and ——, 1983: The water budget of a mesoscale convective system in the tropics. *J. Atmos. Sci.*, **40,** 1835–1850.

Heymsfield, A. J., 1976: Particle size distribution measurement: An evaluation of the Knollenberg optical array probes. *Atmos. Technol.*, **8,** 17–24.

Hobbs, P. V., 1974: *Ice Physics.* Clarendon Press, 803 pp.

Houze, R. A., Jr., 1973: A climatological study of vertical transports by cumulus-scale convection. *J. Atmos. Sci.*, **30,** 1112–1123.

——, 1977: Structure and dynamics of a tropical squall-line system observed during GATE. *Mon. Wea. Rev.*, **105,** 1540–1567.

——, 1982: Cloud clusters and large-scale vertical motions in the tropics. *J. Meteor. Soc. Japan,* **60,** 396–414.

——, and A. K. Betts, 1981: Convection in GATE. *Rev. Geophys. Space Phys.*, **19,** 541–576.

——, and P. V. Hobbs, 1982: Organization and structure of precipitating cloud systems. *Advances in Geophysics,* Vol. 24, Academic Press 225–315.

——, and E. N. Rappaport, 1984: Air motions and precipitation structure of an early summer squall line over the eastern tropical Atlantic. *J. Atmos. Sci.*, **41,** 553–574.

——, S. G. Geotis, F. D. Marks, Jr., D. D. Churchill and P. H. Herzegh, 1981a: Comparison of airborne and land-based radar measurements of precipitation during winter MONEX. *J. Appl. Meteor.*, **20,** 772–783.

——, ——, —— and A. K. West, 1981b: Winter monsoon convection in the vicinity of North Borneo. Part I: Structure and time variation of the clouds and precipitation. *Mon. Wea. Rev.*, **109,** 1595–1614.

Hudlow, M. D., V. Patterson, P. Pytlowany, F. Richards and S. Geotis, 1979: Calibration and intercomparison of the GATE C-band weather radars. NOAA Tech. Rep. EDIS 31, 98 pp. Center for Environmental Assessment Services, NOAA, Washington, DC 20235. [NTIS PB8120305].

Johnson, R. H., 1982: Vertical motion of near-equatorial winter monsoon convection. *J. Meteor. Soc. Japan,* **60,** 682–690.

——, and D. L. Priegnitz, 1981: Winter monsoon convection in the vicinity of North Borneo. Part II: Effects on large-scale fields. *Mon. Wea. Rev.*, **109,** 1615–1628.

Julian, P. R., 1982: The aircraft dropwindsonde system in the global weather experiment. *Bull. Amer. Meteor. Soc.*, **63,** 619–627.

Knollenberg, R. G., 1970: The optical array: An alternative to scattering or extinction for airborne particle size determination. *J. Appl. Meteor.*, **9,** 86–103.

Leary, C. A., 1984: Precipitation structure of the cloud clusters in a tropical easterly wave. *Mon. Wea. Rev.*, **112,** 313–325.

——, and R. A. Houze, Jr., 1979a: The structure and evolution of convection in a tropical cloud cluster. *J. Atmos. Sci.*, **36,** 437–457.

——, and ——, 1979b: Melting and evaporation of hydrometeors in precipitation from the anvil clouds of deep tropical convection. *J. Atmos. Sci.*, **36,** 669–679.

LeMone, M. A., and E. J. Zipser, 1980: Cumulonimbus vertical velocity events in GATE. Part I: Diameter, intensity and mass flux. *J. Atmos. Sci.*, **37,** 2444–2457.

Maddox, R. A., 1980: Mesoscale convective complexes. *Bull. Amer. Meteor. Soc.*, **61,** 1374–1387.

Matejka, T. J., R. A. Houze, Jr. and P. V. Hobbs, 1980: Microphysics and dynamics of clouds associated with mesoscale rainbands in extratropical cyclones. *Quart. J. Roy. Meteor. Soc.*, **106,** 29–56.

Ramage, C. S., 1971: *Monsoon Meteorology.* Academic Press, 271 pp.

Ruskin, R. E., 1976: Liquid water content devices. *Atmos. Technol.*, **8,** 38–42.

Warner, C., 1982: Mesoscale features and cloud organization on 10–12 December 1978 over the South China Sea. *J. Atmos. Sci.*, **39,** 1619–1641.

——, J. Simpson, D. W. Martin, D. Suchman, F. R. Mosher and R. F. Reinking, 1979: Deep convection on day 261 of GATE. *Mon. Wea. Rev.*, **108,** 169–194.

Zipser, E. J., 1969: The role of organized unsaturated convective downdrafts in the structure and rapid decay of an equatorial disturbance. *J. Appl. Meteor.*, **8,** 799–814.

——, 1977: Mesoscale and convective-scale downdrafts as distinct components of squall-line circulation. *Mon. Wea. Rev.*, **105,** 1568–1589.

——, and M. A. LeMone, 1980: Cumulonimbus vertical velocity events in GATE. Part II: Synthesis and model core structure. *J. Atmos. Sci.*, **37,** 2458–2469.

——, R. J. Meitin and M. A. LeMone, 1981: Mesoscale motion fields associated with a slowly moving GATE convective band. *J. Atmos. Sci.*, **38,** 1725–1750.